

# Grid-based calculations of redshift-space matter fluctuations from perturbation theory: UV sensitivity and convergence at the field level

Atsushi Taruya<sup>1,2</sup>, Takahiro Nishimichi<sup>1,2</sup> and Donghui Jeong<sup>3,4</sup>

<sup>1</sup>*Center for Gravitational Physics, Yukawa Institute for Theoretical Physics, Kyoto University, Kyoto 606-8502, Japan*

<sup>2</sup>*Kavli Institute for the Physics and Mathematics of the Universe, Todai Institutes for Advanced Study, the University of Tokyo, Kashiwa, Chiba 277-8583, Japan (Kavli IPMU, WPI)*

<sup>3</sup>*Department of Astronomy and Astrophysics and Institute for Gravitation and the Cosmos, The Pennsylvania State University, University Park, Pennsylvania 16802, USA*

<sup>4</sup>*School of Physics, Korea Institute for Advanced Study (KIAS), 85 Hoegiro, Dongdaemun-gu, Seoul 02455, Republic of Korea*



(Received 24 September 2021; accepted 10 April 2022; published 6 May 2022)

Perturbation theory (PT) has been used to interpret the observed nonlinear large-scale structure statistics in the quasilinear regime. To facilitate the PT-based analysis, we have presented the GridSPT algorithm, a grid-based method to compute the nonlinear density and velocity fields in standard perturbation theory (SPT) from a given linear power spectrum. Here, we expand on this approach by taking the redshift-space distortions into account. With the new implementation, we generate for the first time the redshift-space density field to the fifth order and computed the next-to-next-to-leading-order (two-loop) power spectrum and the next-to-leading-order (one-loop) bispectrum of matter clustering in redshift space. By comparing the result with the corresponding analytical SPT calculation and  $N$ -body simulations, we find that the SPT calculation (A) suffers much more from UV sensitivity due to the higher-derivative operators, and (B) deviates from the  $N$ -body results above the Fourier wave number smaller than real space  $k_{\text{max}}$ . Finally, we show that while the Padé approximation removes spurious features in the morphology, it does not improve the modeling of the power spectrum and bispectrum.

DOI: [10.1103/PhysRevD.105.103507](https://doi.org/10.1103/PhysRevD.105.103507)

## I. INTRODUCTION

Galaxy redshift surveys [1] provide a wealth of cosmological information, which enables us to probe the late-time cosmic expansion history as well as the growth of large-scale structure. They also offer a clue to probe primordial fluctuations, from which one can address the fundamental physics questions of the early Universe. In addition to several ongoing ground-based surveys such as HETDEX [2], PFS [3], and DESI [4], there are space-based missions planned to probe galaxies out to higher redshifts over a large sky area, such as Euclid<sup>1</sup> [5], the Nancy Grace Roman Space Telescope<sup>2</sup> [6], and SPHEREx<sup>3</sup> [7]. These gigantic surveys aim to dramatically improve our understanding of the Universe, and resolve puzzles such as the nature of dark matter and dark energy and the physics of cosmic inflation.

Surveying a larger volume with a higher galaxy number density means that these surveys measure the summary statistics—such as the power spectrum and correlation function—with unprecedented precision, and this can offer

a tight constraint on cosmological parameters, helping us to clarify the nature of cosmic acceleration as well as to test gravity on cosmological scales [8]. In doing so, it is indispensable to obtain an accurate theoretical description of the large-scale structure along with the observational systematics. In galaxy surveys, major systematics that need to be controlled are the nonlinearities in gravitational evolution, galaxy bias, and redshift-space distortions (RSDs). There have been tremendous efforts to describe these effects both from analytical treatments and numerical simulations, and it is indeed one of the major subjects in observational cosmology (e.g., Refs. [1,9–24]).

Among various techniques and methods, cosmological  $N$ -body simulations and perturbation theory calculations are the standard theoretical tools to accurately predict the observed large-scale structure. In particular,  $N$ -body simulations are powerful in quantitatively describing the clustering of dark matter and halos in the nonlinear regime. Providing a real-space realization of halos,  $N$ -body simulations also make it possible to directly account for the observational systematics, such as the survey window function and masks. On the other hand, the perturbation theory (PT) treatment [25] provides a faster way to predict

<sup>1</sup><https://sci.esa.int/web/euclid>.

<sup>2</sup><https://roman.gsfc.nasa.gov/>.

<sup>3</sup><https://spherex.caltech.edu/>.

statistical quantities in the weakly nonlinear regime, and is used as a theoretical template of the measured power spectrum or correlation function. These two approaches are complementary, and a combination of them may give a more efficient theoretical tool with versatile applications (e.g., Ref. [23]).

To facilitate the PT-based approach, we have developed a grid-based algorithm to *simulate* the nonlinear density and velocity fields of large-scale structure, based on the standard perturbation theory (SPT) [26] (see Refs. [27,28] for earlier works). Taking advantage of the fast Fourier transform (FFT), its C++ implementation, called GridSPT, enables us to quickly generate the nonlinearly evolved density and velocity fields at each order in SPT. Then, we can apply all analysis tools developed for the statistical analysis of the density and velocity fields on configuration-space grids, for example, for  $N$ -body simulations or for the analysis of survey data. Furthermore, the observational systematics such as the survey window function and masks can be easily incorporated into the grid density fields. As an explicit demonstration, in Ref. [29] we estimated the covariance matrix of the matter power spectrum with various shapes of survey window functions, including the higher-order corrections from the next-to-leading-order (one-loop) trispectrum.

In this paper, extending the previous grid-based algorithm to include the RSDs [30,31], we present an explicit implementation of the RSD effects in GridSPT. Previous studies, for example in Refs. [14,18] and Ref. [32], have shown that the *naive* SPT calculation of the matter power spectrum in redshift space does not provide as good of a model as that in real space, and there have been numerous works to improve the SPT predictions (e.g., Refs. [14,18,33–41]). Making use of the grid-based treatment, we will see how the naive SPT treatment leads to an inaccurate prediction particularly at the field level, even after including the nonlinear corrections up to the fifth order. Also, applying the Padé approximations to the SPT density fields, we will look for the possibility of using a resummed treatment for more accurate modeling. It is, however, to be stressed that the implementation of the RSD effect in GridSPT is not our final goal. In future work we plan to implement the effect of galaxy bias as well as the effective-field-theory treatment (e.g., Refs. [20,42–44]), the latter of which can mitigate the UV-sensitive behaviors of the SPT calculation, and we thus expect that the method has the potential to improve upon the SPT predictions. Note that GridSPT algorithm was applied to a precise calibration of the effective-field-theory counterterms for the bispectrum and trispectrum at next-to-leading order [45,46].

In principle, one can implement the RSD effect from the GridSPT output by mapping the real-space density field to redshift space using the line-of-sight component of the peculiar velocity field. However, a naive implementation of

the mapping formula in grid space needs an interpolation, for which an accurate computation needs a nonperturbative calculation. For the perturbative treatment, we present a novel expression that relates the redshift-space density field in terms of the real-space density and velocity fields. We then evaluate the expression at the redshift-space position. In this way, no interpolation technique is necessary, and one can directly *reconstruct* the SPT density field in redshift space from the real-space GridSPT calculations. With an explicit implementation of the RSD effects, we investigate the statistical and morphological properties of the redshift-space SPT density fields.

The organization of this paper is as follows. In Sec. II we begin by briefly reviewing the grid-based SPT calculation of large-scale structure, and comment on the aliasing effect that appears in a practical implementation. Then, in Sec. III we consider the RSD, and derive the expression for the redshift-space density field written in terms of real-space quantities. Based on this, we present a perturbative framework to compute density fields with GridSPT. Section IV presents an explicit demonstration of GridSPT calculations taking the RSD effect into account, for which we also make a detailed comparison with  $N$ -body simulations and analytical SPT calculations. To this end, we present for the first time the two-loop SPT power spectrum in redshift space. Section V discusses the application of Padé approximations to GridSPT and discusses the possibility to improve the SPT calculations in redshift space at the field level. Finally, Sec. VI is devoted to the conclusion and discussions of future prospects.

Throughout the paper, we use the following Fourier convention:

$$f(\mathbf{k}) = \int d^3x e^{-i\mathbf{k}\cdot\mathbf{x}} f(\mathbf{x}), \quad (1)$$

$$f(\mathbf{x}) = \int \frac{d^3k}{(2\pi)^3} e^{i\mathbf{k}\cdot\mathbf{x}} f(\mathbf{k}) \equiv \int_{\mathbf{k}} e^{i\mathbf{k}\cdot\mathbf{x}} f(\mathbf{k}). \quad (2)$$

## II. GRID-BASED PERTURBATION THEORY

In this section, we present a concise review of the grid-based calculation for perturbation theory of large-scale structure called GridSPT described in Ref. [26]. In essence, GridSPT enables us to perform SPT calculations at the field level, and to generate the numerical realizations of higher-order density and velocity fields at each grid point. The heart of the algorithm is the real-space recursion relation in Eq. (6), upon which the GridSPT implementation is based.

Standard perturbation theory models the gravitational evolution of a matter distribution by integrating the Vlasov-Poisson equations under the assumption of single-stream matter flow [25]. In this framework, the large-scale matter distribution is described by the pressureless fluid equations

coupled with the Poisson equation. When further combined with the irrotational flow assumption, which is also valid on large scales, the system of equations describing the nonlinear evolution of density and velocity fields is further reduced to

$$\frac{d}{d\eta} \begin{pmatrix} \delta \\ \theta \end{pmatrix} + \Omega_{ab} \begin{pmatrix} \delta \\ \theta \end{pmatrix} = \begin{pmatrix} \nabla \cdot [\delta \mathbf{u}] \\ \nabla \cdot [(\mathbf{u} \cdot \nabla) \mathbf{u}] \end{pmatrix}, \quad (3)$$

where we introduce the time variable  $\eta$  defined by  $\eta \equiv \ln D_+(t)$ , with  $D_+$  being the linear growth factor. We denote the comoving coordinate as  $\mathbf{x}$ . The quantities  $\delta = \delta(\mathbf{x}, \eta)$  and  $\theta = \theta(\mathbf{x}, \eta)$  are the mass density and the velocity-divergence fields, respectively. The velocity-divergence field is related to the velocity field  $\mathbf{v}$  through  $\theta \equiv -\nabla \mathbf{v} / (f a H) \equiv \nabla \cdot \mathbf{u}$ , with  $f$  being the linear growth rate, defined by  $f \equiv d \ln D_+ / d \ln a$ . The field  $\mathbf{u}$  is the *reduced* velocity field given by  $\mathbf{u} = \nabla[\nabla^{-2} \theta]$  for an irrotational matter flow. The matrix  $\Omega_{ab} = \Omega_{ab}(\eta)$  generally depends on cosmology and time, but replacing that with the time-independent constant matrix  $\Omega_{ab}^{\text{EdS}}$  for an Einstein–de Sitter universe,

$$\Omega_{ab}^{\text{EdS}} = \begin{pmatrix} 0 & -1 \\ -\frac{3}{2} & \frac{1}{2} \end{pmatrix}, \quad (4)$$

provides a good approximation for a wide class of cosmology models close to  $\Lambda$ CDM (e.g., Refs. [47–49]).

We obtain the perturbative solutions for Eq. (3) by expanding the density and velocity fields. For the dominant growing-mode contributions, we have

$$\delta(\mathbf{x}, \eta) = \sum_n \delta_n(\mathbf{x}, \eta), \quad \theta(\mathbf{x}, \eta) = \sum_n \theta_n(\mathbf{x}, \eta), \quad (5)$$

with the time dependence at each order scaled as  $\delta_n$ ,  $\theta_n \propto e^{m\eta}$ . Hereafter, we suppress arguments of  $\eta$  for the perturbed quantities and simply write  $\delta_n(\mathbf{x})$  and  $\theta_n(\mathbf{x})$ . Substituting Eq. (5) into Eq. (3) and using  $\Omega_{ab}$  in Eq. (4), the order-by-order calculation leads to the following recursion relation [26]:

$$\begin{pmatrix} \delta_n(\mathbf{x}) \\ \theta_n(\mathbf{x}) \end{pmatrix} = \frac{2}{(2n+3)(n-1)} \begin{pmatrix} n + \frac{1}{2} & 1 \\ \frac{3}{2} & n \end{pmatrix} \times \sum_{m=1}^{n-1} \begin{pmatrix} (\nabla \delta_m) \cdot \mathbf{u}_{n-m} + \delta_m \theta_{n-m} \\ \frac{1}{2} \nabla^2 (\mathbf{u}_m \cdot \mathbf{u}_{n-m}) \end{pmatrix}, \quad (6)$$

for  $n \geq 2$ . Here we have used the identity  $\nabla \cdot [(\mathbf{u} \cdot \nabla) \mathbf{u}] = \frac{1}{2} \nabla^2 (\mathbf{u} \cdot \mathbf{u})$  for an irrotational (curl-free) velocity field  $\mathbf{u}$ . Unlike the equivalent expression given in Ref. [26], Eq. (6) involves no tensor-field calculation, which is helpful for reducing the memory requirement in the numerical

implementation. We complete the recursion relation by using the linear-order ( $n = 1$ ) growing-mode solution

$$\begin{pmatrix} \delta_1(\mathbf{x}) \\ \theta_1(\mathbf{x}) \end{pmatrix} = e^\eta \begin{pmatrix} 1 \\ 1 \end{pmatrix} \delta_0(\mathbf{x}), \quad (7)$$

where  $\delta_0(\mathbf{x})$  is the linear density field given at an initial time.

For a given linear density field  $\delta_0(\mathbf{x})$  on grids, we use them as an initial condition for the recursion [Eq. (7)] to calculate the nonlinear source terms given on the right-hand side of Eq. (6). The FFT facilitates the calculation of the derivative operators  $\nabla_j$ , which simply becomes a multiplication of  $i\mathbf{k}_j$  in Fourier space. We have presented details of the algorithm and implementation in Sec. II C of Ref. [26].<sup>4</sup> In Ref. [26], we generated nonlinear density fields up to fifth order and studied both their morphological and statistical properties in a face-to-face comparison with  $N$ -body simulations that begins from *exactly* the same random realizations. One of the advantages of this method is that grid-based codes for the statistical analysis of  $N$ -body simulation results can be reused for the outcomes of GridSPT, and once the density fields are generated the predictions can be scaled to any redshift analytically by using the fact that the time dependence of the  $n$ th-order fields is simply described as  $\delta_n, \theta_n \propto e^{m\eta}$ .

It is worth noting that the operations for the GridSPT implementation, particularly calculating the right-hand side of Eq. (6), can generate the aliasing effect, which arises when fast Fourier transforming the nonlinear terms evaluated in configuration space (see Appendix A 1). The aliasing effect produces spurious high-wave-number Fourier modes that affect the small-scale behaviors of the resulting nonlinear fields. Mitigating such an effect is thus critical for a practical SPT calculation at the field level.

A simple but widely used technique to mitigate the aliasing effect is to discard the high-frequency modes. In our previous papers [26,29], we adopted the so-called 2/3 rule to set Fourier modes in the high-frequency range of  $k > (2/3)k_{\text{Nyq}}$  to zero at each step of the GridSPT calculation. Here, the wave number  $k_{\text{Nyq}}$  is the Nyquist frequency defined by  $k_{\text{Nyq}} \equiv \pi/L_p$ , where  $L_p \equiv (L_{\text{box}}/N_{\text{grid}}^{1/3})$  is the grid separation, and  $L_{\text{box}}$  and  $N_{\text{grid}}$  are, respectively, the side length and total number of grids for the comoving cubic box inside which the fields  $\delta_n$  and  $\theta_n$  are defined. Strictly speaking, however, the 2/3 rule is valid only for the aliasing effect arising from the quadratic operations of the fields. For nonlinear terms with the  $N$ th power of the fields, however, the 2/3 rule has to be generalized to the  $2/(N+1)$  rule. That is, the modes with

<sup>4</sup>With the real-space recursion relation in Eq. (6), one important difference from the algorithm in Ref. [26] is that we do not need to compute the tensor fields  $\partial_i u_j$  at every step of PT calculations.

wave number  $k > 2/(N+1)k_{\text{Nyq}}$  are to be discarded before the calculation of nonlinear terms. Applying the  $2/(N+1)$  rule has been essential in computing the redshift-space density field with GridSPT since the redshift-space density field is constructed perturbatively with higher powers of the density and velocity fields. In Appendix A, we discuss this point in greater detail and present a comparison among results of the GridSPT calculations with various dealiasing treatments.

Finally, a cautionary remark is in order: the single-stream PT treatment ceases to be adequate in the nonlinear regime where the multistream flow is generated, and recent studies show that the multistream effect on the matter distribution is manifest even on large scales and becomes more significant at higher order (e.g., Refs. [23,50–52]). The effective-field-theory treatment can remedy the situation by introducing counterterms that absorb the UV sensitivity. We will leave a grid-based implementation of the effective-field-theory treatment for our future work, and focus on modeling RSD in the GridSPT framework.

### III. IMPLEMENTING REDSHIFT-SPACE DISTORTIONS IN GridSPT

In this section, based on the standard PT treatment, we present an algorithm to perturbatively compute the redshift-space density fields on grids.

First, recall that the observed position of a galaxy in redshift space,  $s$ , is related to the real-space position  $\mathbf{x}$  through

$$\mathbf{s} = \mathbf{x} - f u_z(\mathbf{x}) \hat{z}, \quad (8)$$

where  $u_z$  is the line-of-sight component of the field  $\mathbf{u}$ , defined earlier as  $\mathbf{u} \equiv -\mathbf{v}/(faH)$ , with  $\mathbf{v}$  being the peculiar velocity. Throughout the paper, we work with the distant-observer limit and take the  $z$  axis as the line-of-sight direction. With the mapping relation in Eq. (8), one finds an expression for the density field in redshift space, denoted by  $\delta^{(S)}$ , in terms of the real-space quantities as (e.g., Refs. [1,32]; see also Refs. [53–55] for the expression without taking the distant-observer limit)

$$\begin{aligned} \delta^{(S)}(\mathbf{s}) &= \left| \frac{\partial \mathbf{s}}{\partial \mathbf{x}} \right|^{-1} \{1 + \delta(\mathbf{x})\} - 1 \\ &= \frac{\delta(\mathbf{x}) + f \nabla_z u_z(\mathbf{x})}{1 - f \nabla_z u_z(\mathbf{x})}, \end{aligned} \quad (9)$$

where the operator  $\nabla_z$  stands for the line-of-sight derivative,  $\hat{z} \cdot \nabla_x$ . The above expression is exact in the distant-observer limit and, using GridSPT, the quantities on the right-hand side can be computed up to an arbitrary order without expanding the denominator. Note, however, that the right-hand side of Eq. (9) is still to be evaluated at the real-space position. In order to obtain the density field in redshift space, we therefore have to transform the quantities at the real-space position  $\mathbf{x}$  to the redshift-space position  $\mathbf{s}$  through Eq. (8). Although such a transformation can be implemented rigorously up to an arbitrary order in PT calculations, the resultant redshift-space density fields no longer reside at the original grids. To obtain a regularly spaced density field, we have to interpolate among the resultant density fields. Such an operation obscures the counting of PT order, so it is incompatible with a PT calculation in a strict sense. We will leave this implementation as a future work.

To circumvent the situation, we derive an alternative expression for the redshift-space density field. To do so, consider the Fourier transform of the redshift-space density field:

$$\begin{aligned} \delta^{(S)}(\mathbf{k}) &= \int d^3 s e^{-ik \cdot s} \delta^{(S)}(\mathbf{s}) \\ &= \int d^3 s e^{-ik \cdot s} \left[ \left| \frac{\partial \mathbf{s}}{\partial \mathbf{x}} \right|^{-1} \{1 + \delta(\mathbf{x})\} - 1 \right] \\ &= \int d^3 \mathbf{x} e^{-ik \cdot (\mathbf{x} - f u_z(\mathbf{x}) \hat{z})} \{ \delta(\mathbf{x}) + f \nabla_z u_z(\mathbf{x}) \}. \end{aligned} \quad (10)$$

In the last line we changed the variable of the integral from  $s$  to  $\mathbf{x}$ , using Eq. (8) and the Jacobian  $|\partial s / \partial \mathbf{x}| = 1 - f \nabla_z u_z(\mathbf{x})$ . Taylor expanding the velocity field in the exponent and substituting the Fourier transform of the quantities  $\delta$  and  $u_z$ , we obtain

$$\begin{aligned} \delta^{(S)}(\mathbf{k}) &= \int d^3 \mathbf{x} e^{-ik \cdot \mathbf{x}} \sum_{n=0}^{\infty} \frac{i^n}{n!} (f k_z)^n \{ \delta(\mathbf{x}) + f \nabla_z u_z(\mathbf{x}) \} \{ u_z(\mathbf{x}) \}^n \\ &= \sum_{n=0}^{\infty} \frac{(f k_z)^n}{n!} \int d^3 \mathbf{x} e^{-ik \cdot \mathbf{x}} \int_{\mathbf{p}} e^{i\mathbf{p} \cdot \mathbf{x}} \int_{\mathbf{q}_1} e^{i\mathbf{q}_1 \cdot \mathbf{x}} \dots \int_{\mathbf{q}_n} e^{i\mathbf{q}_n \cdot \mathbf{x}} \left\{ \delta(\mathbf{p}) + f \frac{p_z^2}{p^2} \theta(\mathbf{p}) \right\} \frac{q_{1,z}}{q_1^2} \theta(\mathbf{q}_1) \dots \frac{q_{n,z}}{q_n^2} \theta(\mathbf{q}_n). \end{aligned} \quad (11)$$

Here, we consider the irrotational velocity flow,<sup>5</sup> and used the velocity-divergence field  $\theta$  [see Eq. (3) above], with which  $u_z(\mathbf{k}) = (-ik_z/k^2)\theta(\mathbf{k})$ .

Going back to configuration space, the inverse Fourier transform of Eq. (11) gives

$$\begin{aligned} \delta^{(S)}(s) &= \int \frac{d^3\mathbf{k}}{(2\pi)^3} e^{i\mathbf{k}\cdot\mathbf{s}} \delta^{(S)}(\mathbf{k}) \\ &= \sum_{n=0} \int_{\mathbf{p}} \int_{\mathbf{q}_1} \dots \int_{\mathbf{q}_n} e^{i(\mathbf{p}+\mathbf{q}_1+\dots+\mathbf{q}_n)\cdot\mathbf{s}} \frac{f^n(p_z + \sum_{i=1}^n q_{i,z})^n}{n!} \left\{ \delta(\mathbf{p}) + f \frac{p_z^2}{p^2} \theta(\mathbf{p}) \right\} \frac{q_{1,z}}{q_1^2} \theta(\mathbf{q}_1) \dots \frac{q_{n,z}}{q_n^2} \theta(\mathbf{q}_n). \end{aligned} \quad (12)$$

Finally, the above expression can be recast as

$$\delta^{(S)}(s) = \sum_{n=0} \frac{f^n}{n!} \tilde{\nabla}_z^n [\{\delta(s) + f \tilde{\nabla}_z u_z(s)\} \{u_z(s)\}^n], \quad (13)$$

with the operator  $\tilde{\nabla}_z$  defined by  $\tilde{\nabla}_z \equiv \hat{z} \cdot \nabla_s$ . Note that the  $\hat{z}$  direction is well defined both in real space and redshift space.

Equation (13) is the key equation to perform a grid-based PT calculation in redshift space. In contrast to Eq. (9), the right-hand side is now expressed as a function of the redshift-space position  $s$ . Hence, we use Eq. (13) as a basis to directly compute the redshift-space density field from the real-space quantities without any interpolation. To be explicit, let us apply the SPT expansion given in Eq. (5), and substitute these expansions in real space into Eq. (13). Perturbatively computing the redshift-space density field, the order-by-order calculation leads to

$$\delta^{(S)} = \sum_{n=1} \delta_n^{(S)}, \quad (14)$$

with the explicit expression of  $\delta_n^{(S)}$  given below up to the fifth order:

$$\delta_1^{(S)} = D_1, \quad (15)$$

$$\delta_2^{(S)} = D_2 + f \tilde{\nabla}_z (D_1 u_{z,1}), \quad (16)$$

$$\delta_3^{(S)} = D_3 + f \tilde{\nabla}_z (D_1 u_{z,2} + D_2 u_{z,1}) + \frac{f^2}{2!} \tilde{\nabla}_z^2 (D_1 u_{z,1}^2), \quad (17)$$

$$\begin{aligned} \delta_4^{(S)} &= D_4 + f \tilde{\nabla}_z (D_1 u_{z,3} + D_2 u_{z,2} + D_3 u_{z,1}) \\ &\quad + \frac{f^2}{2!} \tilde{\nabla}_z^2 (2D_1 u_{z,1} u_{z,2} + D_2 u_{z,1}^2) + \frac{f^3}{3!} \tilde{\nabla}_z^3 (D_1 u_{z,1}^3), \end{aligned} \quad (18)$$

<sup>5</sup>To be precise, in deriving Eq. (13), we do not necessarily assume irrotationality.

$$\begin{aligned} \delta_5^{(S)} &= D_5 + f \tilde{\nabla}_z (D_1 u_{z,4} + D_2 u_{z,3} + D_3 u_{z,2} + D_4 u_{z,1}) \\ &\quad + \frac{f^2}{2!} \tilde{\nabla}_z^2 \{D_1 (2u_{z,1} u_{z,3} + u_{z,2}^2) + 2D_2 u_{z,1} u_{z,2} + D_3 u_{z,1}^2\} \\ &\quad + \frac{f^3}{3!} \tilde{\nabla}_z^3 (3D_1 u_{z,1}^2 u_{z,2} + D_2 u_{z,1}^3) + \frac{f^4}{4!} \tilde{\nabla}_z^4 (D_1 u_{z,1}^4), \end{aligned} \quad (19)$$

where we introduced the perturbed quantity  $D_n$ , defined by

$$D_n \equiv \delta_n + f \tilde{\nabla}_z u_{z,n}. \quad (20)$$

Now, the recipe to compute  $\delta^{(S)}$  with GridSPT is to first evaluate the real-space density and velocity fields,  $\delta$  and  $u_z$ , up to an arbitrary order, and then plug them into the above expressions. All the calculations are done in the same grid space in which we obtained the real-space quantities. Note that, as a matter of course, the Fourier transform of the density field at each order,  $\delta_n^{(S)}(\mathbf{k})$ , yields an identical expression to the one with the redshift-space kernel  $Z_n$  in the literature [see Eq. (B1)].

#### IV. RESULTS

Using the prescription in Sec. III, we are in a position to present the results of GridSPT calculations in redshift space and compare them to the results from  $N$ -body simulations. Here, for the sake of comprehensive study in parallel with our previous works, we adopt the same cosmological parameters as used in Ref. [26], assuming the flat- $\Lambda$ CDM model:  $\Omega_m = 0.279$  for the matter density,  $\Omega_\Lambda = 0.721$  for dark energy with an equation-of-state parameter  $w = -1$ ,  $\Omega_b/\Omega_m = 0.165$  for the baryon fraction,  $h = 0.701$  for the Hubble parameter,  $n_s = 0.96$  for the scalar spectral index, and  $\sigma_8 = 0.8159$  for the normalization of the fluctuation amplitude at  $8 h^{-1}$  Mpc. We then use the results of the cosmological  $N$ -body simulation done in Ref. [26]. The simulation was carried out using the publicly available code GADGET-2 [56], with  $N_{\text{particle}} = 1024^3$  particles in comoving periodic cubes of  $L_{\text{box}} = 1000 h^{-1}$  Mpc, with the initial density field calculated using the 2LPT code [57]. Specifically, we use the output data at  $z = 0$  and 1 to create the redshift-space density field as well as to measure the statistical quantities.

With the same initial seed and cubic box, we perform the GridSPT calculations up to the fifth order. Unless otherwise stated, the number of grids is set to  $N_{\text{grid}} = 1200^3$  as a default setup. To mitigate the aliasing effect, based on the discussion earlier and in Appendix A, we adopt the  $2/(1+5) = 1/3$  rule (instead of the  $2/3$  rule that we adopted in Ref. [26]) with an isotropic sharp- $k$  filter, which is applied only once to the initial density field.

### A. Properties of SPT density fields

Let us begin by looking at the generated density fields in real and redshift space.

Figures 1 and 2 show the 2D slices of the real- (left) and redshift-space (right) density fields at  $z = 0$  obtained from GridSPT and  $N$ -body results, taking the  $z$  axis to be the

line-of-sight direction. Applying the Gaussian filter of radius  $R = 10 h^{-1}$  Mpc, a slice of the  $x - y$  (Fig. 1) and  $x - z$  plane (Fig. 2) is taken, and is averaged over  $10 h^{-1}$  Mpc depth in each plane. In Figs. 1 and 2 the density fields over the entire box are shown. On the other hand, Figs. 3 and 4 plot a zoomed-in view over the  $200 \times 200 h^{-1}$  Mpc-sized region, which are taken from Figs. 1 and 2 enclosed by the dashed line in the bottom right panel. In all figures, the amplitudes of density fields, plotted on a linear scale, are indicated by the same color scale.

In each panel, the five successive subpanels from top left to bottom middle show the GridSPT results by summing up higher-order corrections one by one, i.e.,  $\sum_{j=1}^n \delta_j$  or  $\sum_{j=1}^n \delta_j^{(S)}$ , with the number  $n$  indicated in each subpanel. These are compared with the  $N$ -body results shown in the

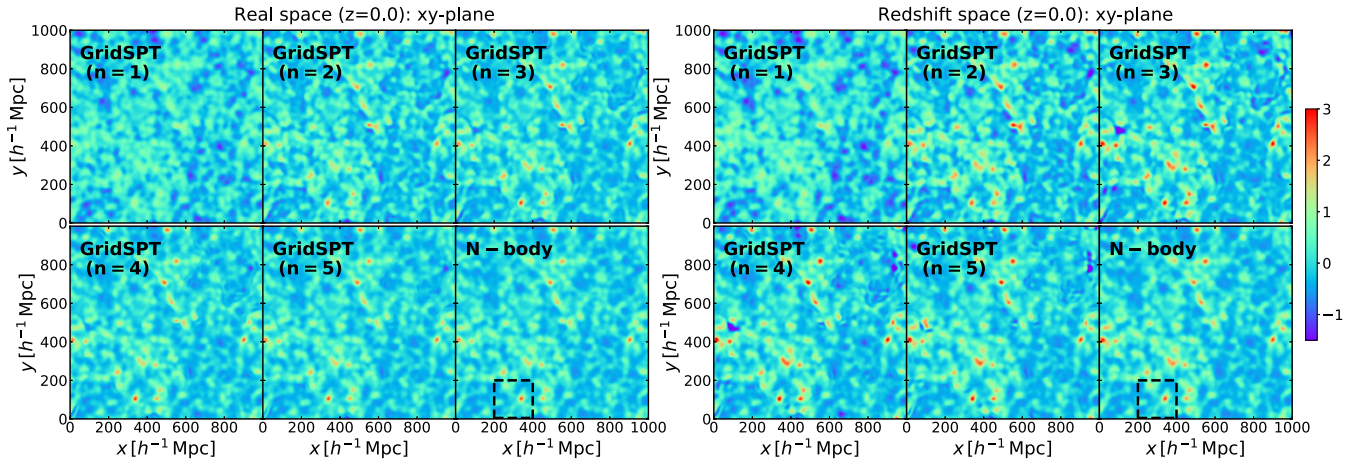


FIG. 1. 2D density field at  $z = 0$  smoothed with a Gaussian filter of  $R = 10 h^{-1}$  Mpc. A slice of the  $x - y$  plane is taken, and the density field averaged over  $10 h^{-1}$  Mpc depth is shown. The left and right panels represent the results in real and redshift space, respectively. In each panel, the results generated with the GridSPT code are shown (from top left to bottom middle). Here, the color scale represents the amplitude of the density field,  $\delta_{\text{SPT}} = \sum_{j=1}^n \delta_j$  or  $\delta_{\text{SPT}}^{(S)} = \sum_{j=1}^n \delta_j^{(S)}$ , with the number  $n$  indicated in each panel. For comparison, the bottom right panel shows the density field from  $N$ -body simulations, evolved with the same initial condition as used in GridSPT calculations.

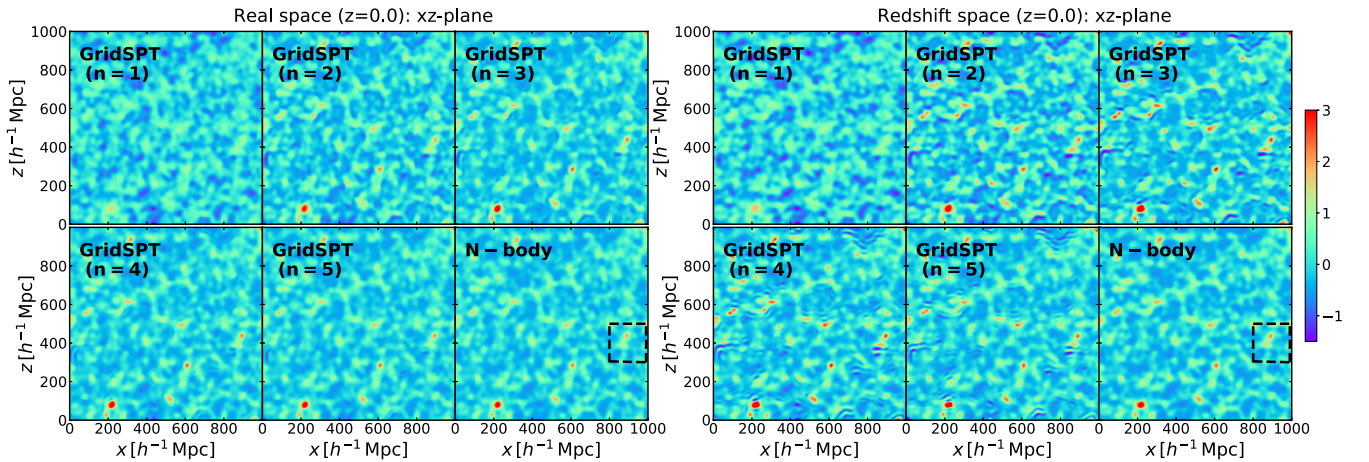


FIG. 2. Same as Fig. 1, but for a slice of  $10 h^{-1}$  Mpc depth in the  $x - z$  plane.

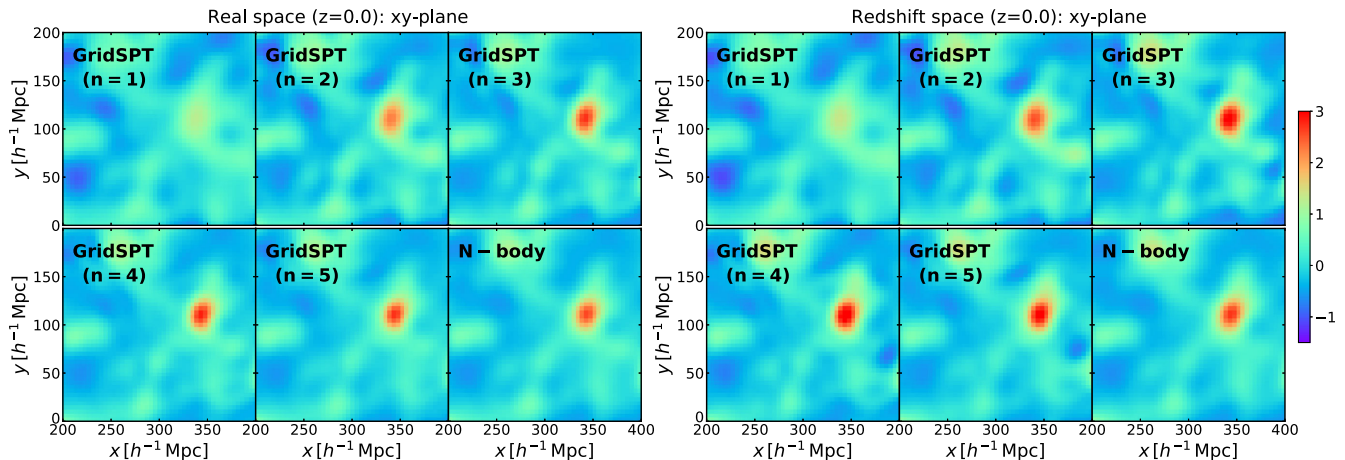


FIG. 3. Same as Fig. 1, but an enlarged plot of the 2D density field with a size of  $200 \times 200 h^{-1} \text{ Mpc}$  is shown for the region enclosed by the dashed line in the bottom right panel of Fig. 1.

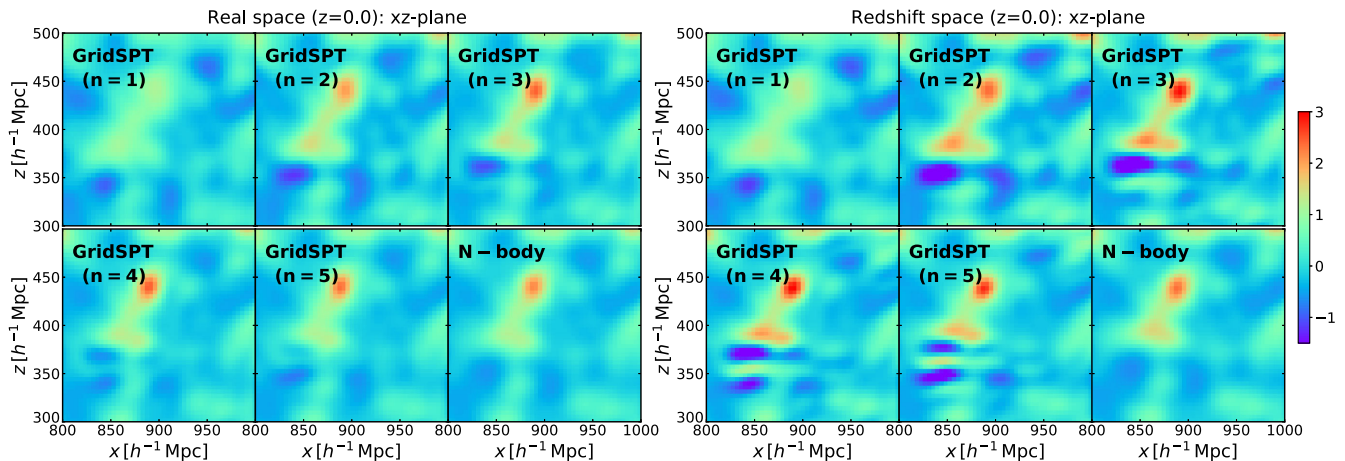


FIG. 4. Same as Fig. 2, but an enlarged plot of the 2D density field over  $200 \times 200 h^{-1} \text{ Mpc}$  size is shown for the region enclosed by the dashed line in the bottom right panel of Fig. 2.

bottom right subpanel. Note that the real-space results in the left panels of Figs. 1 and 3 are exactly the same as Figs. 1 and 2 of Ref. [26], but with a different color scheme. Adding higher-order PT corrections, the real-space density fields obtained from GridSPT get closer to the  $N$ -body result, and at the fifth order the PT density field smoothed over  $10 h^{-1} \text{ Mpc}$  agrees well with the  $N$ -body result.

Similarly, the  $x$ - $y$  plane density fields (Figs. 1 and 3) in redshift space show a good agreement between the fifth-order PT result and the  $N$ -body result. A closer look at the amplitude reveals that the contrast between under- and overdense regions is more pronounced in redshift space. This could be partly ascribed to the Kaiser effect [53,58], but the fact that the effect looks more significant in higher-order GridSPT and  $N$ -body density fields implies that there is some degree of nonlinear contribution, boosting the linear-order enhancement.

On the other hand, in the  $x$ - $z$  plane (Figs. 2 and 3), the GridSPT density fields exhibit wobbly structures with successive under- and overdense regions, which appear most significant along the line-of-sight direction [e.g., see the region around  $(x, z) = (850, 350) h^{-1} \text{ Mpc}$  in the right panels of Fig. 2 or 4]. We have found that those structures are typically found around the underdense regions in the  $N$ -body results. We ascribe this feature to the higher-derivative terms in the higher-order SPT density field [see Eqs. (17)–(19)], based on the fact that such a structure is not seen in the real-space results, and that the feature becomes more prominent as we increase the PT order in redshift space. In particular, the GridSPT implementation requires evaluating the higher-order derivative operator  $\nabla_z^n$ , and we calculate them in Fourier space by multiplying by the factor  $(ik_z)^n$ , which might enhance the aliasing effect beyond the level remedied by the  $2/(N+1)$  rule. We also check that even when implementing the higher-order differential

scheme (e.g., see Appendix C of Ref. [59]) the results are hardly changed. Thus, fake wobbly structures in the  $x$ - $z$  plane are a direct result of our implementation of SPT involving higher-order derivatives. As a result, the overall agreement between GridSPT and  $N$ -body simulations in redshift space is not as good as that in real space even at the fifth order, indicating a slower convergence of the SPT expansion in redshift space. We will discuss this point in more detail from the statistical point of view in the next subsection.

## B. Power spectrum and bispectrum

Inspecting the density fields on grids, we next consider the statistical quantities, in particular focusing on the power spectrum and the bispectrum of the matter field. In both GridSPT and  $N$ -body simulations, we measure them with the same grid-based codes using FFT.<sup>6</sup> In redshift space, the statistical isotropy is known to be manifestly broken, and measured results of the power spectrum and bispectrum, which we respectively denote by  $P^{(S)}$  and  $B^{(S)}$ , exhibit anisotropies along the line-of-sight direction ( $z$  axis in our case). To characterize their anisotropic nature, we apply the multipole expansion and define the multipole moments as

$$P_\ell^{(S)}(k) \equiv \frac{2\ell + 1}{2} \int_{-1}^1 d\mu P^{(S)}(\mathbf{k}) \mathcal{P}_\ell(\mu) \quad (21)$$

for the power spectrum. The function  $\mathcal{P}_\ell$  is the Legendre polynomials, and the quantity  $\mu$  is the directional cosine given by  $\mu \equiv \hat{\mathbf{k}} \cdot \hat{\mathbf{z}}$  or, equivalently,  $k_z/k$  in our setup. For the bispectrum, we adopt the definition used in Ref. [61]:

$$B_\ell^{(S)}(k_1, k_2, k_3) \equiv \frac{2\ell + 1}{2} \int_{-1}^1 d\mu \int_0^{2\pi} \frac{d\phi}{2\pi} B^{(S)}(\mathbf{k}_1, \mathbf{k}_2, \mathbf{k}_3) \mathcal{P}_\ell(\mu), \quad (22)$$

where the directional cosine  $\mu$  is defined with the orientation angle between the line-of-sight direction and the vector normal to the triangle formed with three wave vectors. The angle  $\phi$  represents the azimuthal angle characterizing the rotation of the triangle in the plane. To be specific, we set

$$\mu = \cos \omega = \frac{(\hat{\mathbf{k}}_1 \times \hat{\mathbf{k}}_2) \cdot \hat{\mathbf{z}}}{\sin \theta_{12}}, \quad (23)$$

<sup>6</sup>To be precise, in the case of  $N$ -body simulations, we first assign  $N$ -body particles on grids to generate the density fields. We here adopt the cloud-in-cell (CIC) interpolation to do this. The interlacing dealiasing correction is made based on Ref. [60] before we divide by the CIC window function to obtain our final estimate of the density field on grids.

$$\cos \phi = \frac{\{\hat{\mathbf{z}} \times (\hat{\mathbf{k}}_1 \times \hat{\mathbf{k}}_2)\} \cdot \hat{\mathbf{k}}_1}{\sin \omega}. \quad (24)$$

Note that the bispectrum multipoles  $B^{(S)}$  defined above differ from those used in the literature (e.g., Refs. [62–65]; see also Ref. [66] for a comparison between different coordinate choices), but a nice property of this definition is that they are symmetric under the permutation of the order of  $k_1$ ,  $k_2$ , and  $k_3$ .

Figures 5 and 6 show the results for the matter power spectrum and matter bispectrum from a single realization at  $z = 1$ . Here the bispectrum is measured in the equilateral configuration, taking the three wave numbers to be the same ( $k_1 = k_2 = k_3 \equiv k$ ), and is plotted as a function of  $k$ . The GridSPT results (solid lines) are constructed up to the two-loop and one-loop order, respectively, through

$$P^{(S)}(\mathbf{k}) = P_{\text{lin}}^{(S)}(\mathbf{k}) + P_{1\text{-loop}}^{(S)}(\mathbf{k}) + P_{2\text{-loop}}^{(S)}(\mathbf{k}), \quad (25)$$

$$P_{\text{lin}}^{(S)}(\mathbf{k}) = P_{11}^{(S)}(\mathbf{k}), \quad (26)$$

$$P_{1\text{-loop}}^{(S)}(\mathbf{k}) = 2P_{13}^{(S)}(\mathbf{k}) + P_{22}^{(S)}(\mathbf{k}), \quad (27)$$

$$P_{2\text{-loop}}^{(S)}(\mathbf{k}) = 2P_{15}^{(S)}(\mathbf{k}) + 2P_{24}^{(S)}(\mathbf{k}) + P_{33}^{(S)}(\mathbf{k}) \quad (28)$$

for the power spectrum, and

$$B^{(S)}(\mathbf{k}_1, \mathbf{k}_2, \mathbf{k}_3) = B_{\text{tree}}^{(S)}(\mathbf{k}_1, \mathbf{k}_2, \mathbf{k}_3) + B_{1\text{-loop}}^{(S)}(\mathbf{k}_1, \mathbf{k}_2, \mathbf{k}_3), \quad (29)$$

$$B_{\text{tree}}^{(S)}(\mathbf{k}_1, \mathbf{k}_2, \mathbf{k}_3) = B_{112}^{(S)}(\mathbf{k}_1, \mathbf{k}_2, \mathbf{k}_3) + 2\text{perms}(\mathbf{k}_1 \leftrightarrow \mathbf{k}_2 \leftrightarrow \mathbf{k}_3), \quad (30)$$

$$B_{1\text{-loop}}^{(S)}(\mathbf{k}_1, \mathbf{k}_2, \mathbf{k}_3) = \{B_{123}^{(S)}(\mathbf{k}_1, \mathbf{k}_2, \mathbf{k}_3) + 5\text{perms}(\mathbf{k}_1 \leftrightarrow \mathbf{k}_2 \leftrightarrow \mathbf{k}_3)\} + \{B_{114}^{(S)}(\mathbf{k}_1, \mathbf{k}_2, \mathbf{k}_3) + 2\text{perms}(\mathbf{k}_1 \leftrightarrow \mathbf{k}_2 \leftrightarrow \mathbf{k}_3)\} + B_{222}^{(S)}(\mathbf{k}_1, \mathbf{k}_2, \mathbf{k}_3) \quad (31)$$

for the bispectrum. In the above, the building blocks of the power spectrum and bispectrum,  $P_{ab}$  and  $B_{abc}$ , are defined, respectively, by

$$\langle \delta_a^{(S)}(\mathbf{k}) \delta_b^{(S)}(\mathbf{k}') \rangle = (2\pi)^3 \delta_{\text{D}}(\mathbf{k} + \mathbf{k}') P_{ab}^{(S)}(\mathbf{k}), \quad (32)$$

$$\langle \delta_a^{(S)}(\mathbf{k}_1) \delta_b^{(S)}(\mathbf{k}_2) \delta_c^{(S)}(\mathbf{k}_3) \rangle = (2\pi)^3 \delta_{\text{D}}(\mathbf{k}_1 + \mathbf{k}_2 + \mathbf{k}_3) B_{abc}^{(S)}(\mathbf{k}_1, \mathbf{k}_2, \mathbf{k}_3). \quad (33)$$

Applying the multipole expansion to each term, the multipole moments of the redshift-space power spectrum and bispectrum are evaluated up to  $\ell = 4$  and  $\ell = 2$ ,

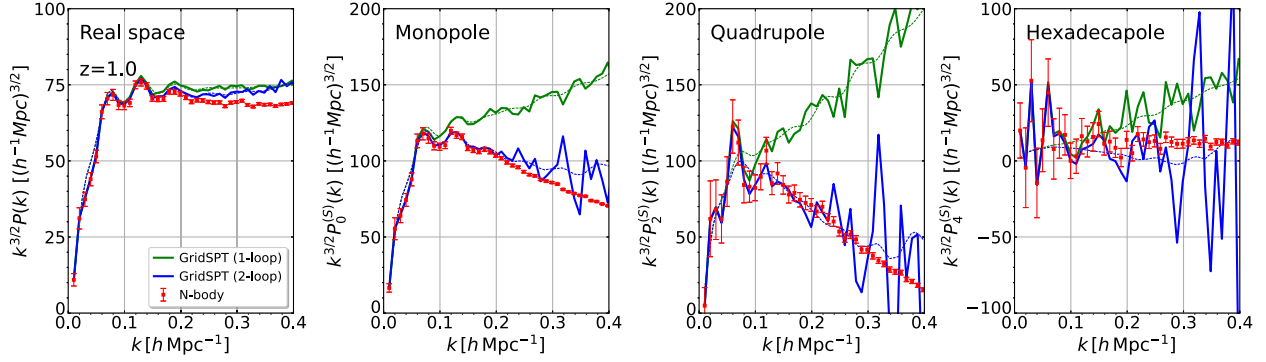


FIG. 5. Power spectrum in real (left) and redshift space (from second left to right) at  $z = 1$ , multiplied by  $k^{3/2}$ . Solid lines are the results from the GridSPT calculation with the number of grids  $N_{\text{grid}} = 1200^3$ . The analytical SPT results are also shown for reference, depicted as dotted lines. Note that the cutoff scale of  $k_{\text{cut}} = 1.4 h \text{ Mpc}^{-1}$  is introduced in the analytical SPT calculations. In both cases, the green and blue curves, respectively, indicate the results at one- and two-loop order. On the other hand, the red symbols represent the measured result from  $N$ -body simulations with the same initial seed as used in GridSPT. Note that the error bars shown in  $N$ -body results are the sampling noise estimated from the number of Fourier modes.

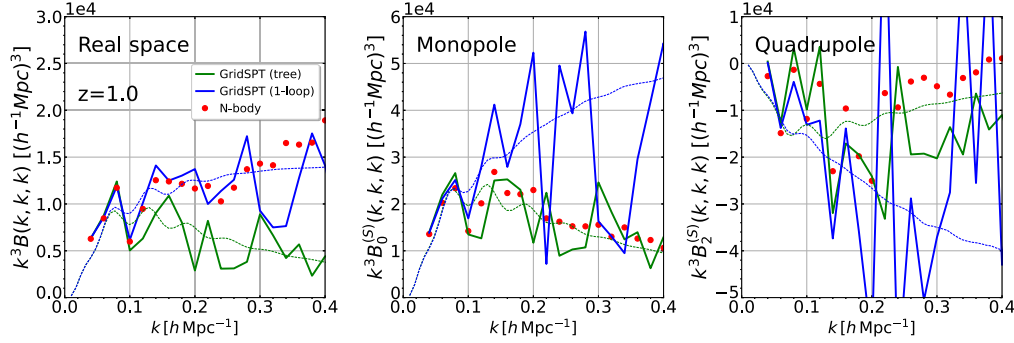


FIG. 6. Bispectrum in real (left) and redshift space (middle and right) at  $z = 1$ , with the number of grids  $N = 1200^3$  in GridSPT calculations. The GridSPT results in the equilateral configuration (i.e.,  $k_1 = k_2 = k_3 \equiv k$ ), depicted as thick solid lines, are plotted as a function of  $k$ . The analytical SPT results are also plotted for reference as dotted lines. In both cases, tree-level and one-loop results are depicted as green and blue curves, respectively. The red filled circles are the measured results of the bispectrum obtained from  $N$ -body simulations. Note that all of the bispectra are multiplied by  $k^3$ .

respectively, together with the real-space power spectrum and bispectrum.<sup>7</sup>

In Figs. 5 and 6 we plot the measurements from the  $N$ -body simulation as red symbols. The error bars shown for the power spectra indicate the sampling noise estimated from the number of Fourier modes in each bin. In addition, we plot the analytical SPT predictions, which we obtain by directly performing the relevant loop integrals numerically, at both next-to-leading (one-loop) and next-to-next-to-leading (two-loop) orders (dotted lines). In Appendix B, for the sake of completeness, we present the analytical expressions for the SPT power spectrum and bispectrum in redshift space. Note that in both GridSPT and analytical

SPT calculations, the two-loop redshift-space power spectra are the results presented for the first time in this paper.

Overall, the GridSPT power spectra consistently reproduce the analytical SPT calculations. Note here that for analytical SPT calculations, we introduce the cutoff scales in the linear power spectrum so as to accommodate GridSPT calculations.<sup>8</sup> Compared to the real-space results, adding the two-loop corrections to the one-loop spectra largely suppresses the amplitude of the power spectra. As a result, the predictions at  $z = 1$  get closer to the  $N$ -body results at  $k \lesssim 0.2 h \text{ Mpc}^{-1}$ , above which the GridSPT results become slightly noisier. Note that this does not simply imply that the

<sup>7</sup>In practice, measurements from the density fields on grids are made with discrete Fourier modes, and we use the FFT-based algorithm to directly evaluate the power spectrum and bispectrum multipoles (e.g., Refs. [63,67,68]).

<sup>8</sup>To be precise, we introduce the low- $k$  cutoff  $k_{\text{min}}$  set to the fundamental mode determined by the box size (i.e.,  $k_{\text{min}} = 2\pi/L$ ). Further, the high- $k$  cutoff is introduced, setting  $k_{\text{cut}}$  to  $1.4 h \text{ Mpc}^{-1}$ , which is close to the dealiasing filter scale in GridSPT  $k_{\text{crit}} = k_{\text{Nyq}}/3 \simeq 1.26 h \text{ Mpc}^{-1}$ .

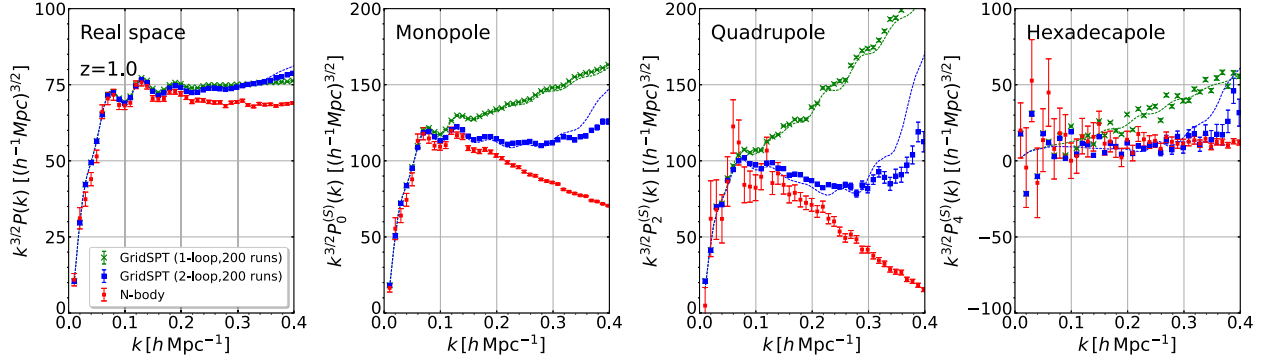


FIG. 7. Same as Fig. 5, but for the GridSPT results at one- and two-loop order (green and blue symbols, respectively), averaged over 200 realizations and adopting the number of grids  $N_{\text{grid}} = 600^3$ . The analytical SPT results (dotted lines) are computed with the cutoff scale  $k_{\text{cut}} = 0.8h \text{ Mpc}^{-1}$ . The error bars on the GridSPT results indicate the standard error of the mean over the 200 realizations. The  $N$ -body results (red symbols) are identical to those shown in Fig. 5, and their error bars indicate the sampling error estimated from the number of Fourier modes for a single realization data. Note that the analytical SPT results shown here (dotted) adopt a different cutoff wave number (see footnote), and thus differ from those in Fig. 5.

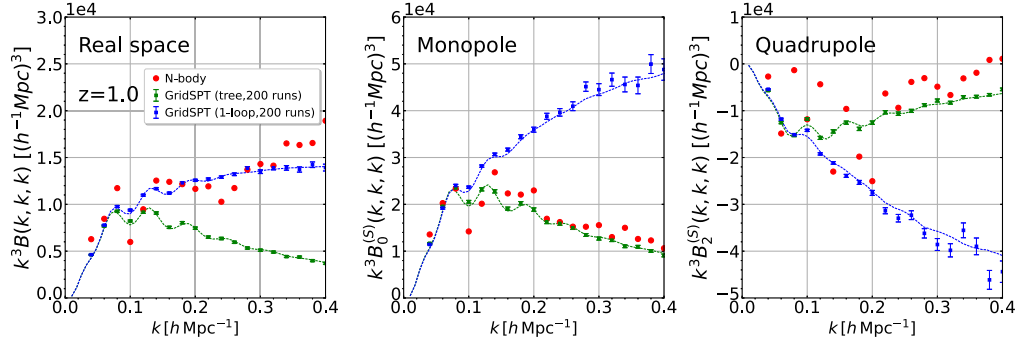


FIG. 8. Same as Fig. 6, but for the GridSPT results of tree-level and one-loop calculations (green and blue symbols, respectively), averaged over 200 realizations and adopting the number of grids  $N_{\text{grid}} = 600^3$ . The error bars for the GridSPT results represent the standard error of the mean over the 200 realizations.

two-loop SPT corrections are essential in predicting the redshift-space power spectra. Indeed, in Appendix E we examine the effective-field-theory treatment and show that adding the counterterms to the GridSPT at one-loop order reasonably reproduces the  $N$ -body results.

On the other hand, adding the one-loop corrections to the monopole and quadrupole, the SPT predictions of the bispectrum positively and negatively increase their amplitudes, respectively. While the one-loop prediction seems to reasonably match the real-space results in  $N$ -body simulations, a quick look at the redshift-space results indicates, that rather than the one-loop SPT, the tree-level predictions better explain the  $N$ -body results. Although these are qualitatively similar to what was found in previous works (e.g., Ref. [61]), the bispectrum measured from the GridSPT fields is rather noisy and it is difficult to judge whether it is quantitatively consistent.

For a more quantitative assessment of the statistical predictions, we increase the number of realizations in GridSPT calculations up to 200, and in Figs. 7 and 8

the averages over the realizations are shown, with the error bars of the GridSPT results indicating the standard error of the mean over 200 realizations. To speed up the calculations, here we adopt a smaller number of grid points,  $N_{\text{grid}} = 600^3$ . In Appendix E the results of their one-loop power spectra are also used to study the impact of the effective-field-theory counterterms. It is now clear that the GridSPT results agree well with analytical SPT predictions for not only the power spectrum but also the bispectrum. Note that the cutoff scales of the analytical SPT calculations were adjusted again so as to get closer to the one introduced in the GridSPT calculations.<sup>9</sup> Then, in redshift space the one-loop bispectra are shown to largely deviate from  $N$ -body simulations, and instead the tree-level

<sup>9</sup>In this case, while the low- $k$  cutoff is kept fixed to the one used in Figs. 5 and 6, the high- $k$  cutoff is changed to  $k_{\text{cut}} = 0.8h \text{ Mpc}^{-1}$ . Note that by adopting  $N_{\text{grid}} = 600^3$ , the dealiasing filter scale of the GridSPT calculations is  $k_{\text{crit}} \simeq 0.62h \text{ Mpc}^{-1}$ .

bispectra match the  $N$ -body results (Fig. 8), in marked contrast to the real-space bispectrum. These are fully consistent with previous results.

Finally, going back to the results of the power spectra in Fig. 7, we find that the agreement between the SPT predictions and  $N$ -body simulations gets worse, compared to the single-realization results in Fig. 5. The discrepancy is particularly manifest and significant at small scales for the monopole and quadrupole moments. The major reason for this comes from the resolution of the GridSPT calculations, originating from the UV sensitivity inherent in the SPT.<sup>10</sup> Indeed, as discussed in detail in Appendix C, the SPT predictions of redshift-space power spectra sensitively depend on the small-scale cutoff. Reducing the high- $k$  cutoff significantly enhances the power spectrum amplitude on small scales. Another point to be noted is the generic feature in the SPT predictions that an oscillatory feature, arising from the baryon acoustic oscillations [69,70], still remains prominent even beyond the scale where the predictions start to deviate from  $N$ -body simulations. This would be a potential concern when improving the GridSPT predictions with the effective-field-theory treatment, and the implementation of the so-called IR resummation could be crucial (see Appendix E).

### C. Cross correlation

So far, comparisons between the GridSPT calculations and  $N$ -body simulations have been made by presenting their respective predictions. In this subsection, we evaluate the cross correlation between their density fields, and statistically investigate the (dis)similarity of the fields evolved using these different techniques starting from the same initial seed.

Consider first the density field at each PT order of GridSPT and compute its cross correlation with the density field obtained from the  $N$ -body simulation. Following Ref. [26], we define the cross-correlation coefficient  $r_{\text{corr}}^{(n)}$  as

$$r_{\text{corr}}^{(n)}(k) \equiv \frac{P_{0,n \times N\text{-body}}^{(S)}(k)}{\sqrt{P_{0,nn}^{(S)}(k)P_{0,N\text{-body}}^{(S)}(k)}}. \quad (34)$$

Here, the quantity in the numerator,  $P_{0,n \times N\text{-body}}^{(S)}$ , represents the monopole moment of the cross power spectrum between the  $n$ th-order SPT density field and the measurement from the  $N$ -body simulation, defined by

$$\langle \delta_n^{(S)}(\mathbf{k}) \delta_{N\text{-body}}^{(S)}(\mathbf{k}') \rangle = (2\pi^3) \delta_{\text{D}}(\mathbf{k} + \mathbf{k}') P_{n \times N\text{-body}}^{(S)}(\mathbf{k}). \quad (35)$$

In the presence of the RSD effect, the above spectrum exhibits anisotropies, for which we take only the monopole moment to evaluate Eq. (34), i.e., averaged over the wave vectors in spherical bins. In Fig. 9 the results in redshift and real space (solid and dotted lines, respectively) are shown up to the fifth order ( $n = 5$ ) at redshifts  $z = 1$  (left) and 0 (right). Note that the real-space results are identical to those obtained in Ref. [26]. While the low- $k$  behaviors exhibit a nonmonotonic scale dependence having a positive or negative value depending on the perturbative order, all of the cross-correlation coefficients asymptotically go to zero at high  $k$ . In real space, it has been suggested in Ref. [26] that the asymptotic convergence at high  $k$  comes from the randomness of the linear displacement field, and this is quantitatively predicted by the analytical treatment with resummed PT calculations [71]. Note that in the Lagrangian PT approach this effect is automatically included, and to describe galaxy/halo density fields perturbatively the IR resummation technique has been developed at the field level [72–74]. Qualitatively, the results in redshift space show similar trends, but a closer look at small scales reveals that the asymptotic convergence to zero seems faster than that in real space, implying that the convergence of the SPT expansion gets worse in redshift space, as we expected.

To elucidate this point more clearly, we next compute the cross-correlation coefficient by summing up each PT correction up to  $n$ th order,  $R_{\text{corr}}^{(n)}$ , defined by

$$R_{\text{corr}}^{(n)}(k) = \frac{\sum_{a=1}^n P_{0,a \times N\text{-body}}^{(S)}(k)}{\sqrt{\{\sum_{a,b=1}^n P_{0,ab}^{(S)}(k)\} P_{0,N\text{-body}}^{(S)}(k)}}. \quad (36)$$

Here, the summation in the denominator is taken only when the expectation values are nonvanishing, that is, only for even numbers of  $a + b$ . The measured results of  $R_{\text{corr}}^{(n)}$  are plotted up to  $n = 5$  in Fig. 10, where we adopt the same color scheme and line types as in Fig. 9. As anticipated, the correlation coefficient in redshift space starts to be suppressed at larger scales, and the suppression appears more rapidly, compared to the results in real space. These features are more prominent at  $z = 0$ . It is also to be noted that adding higher-order SPT corrections does not always improve the cross correlation. At  $n > 3$ , the correlation with  $N$ -body simulation is suppressed significantly at  $k \gtrsim 0.2h \text{ Mpc}^{-1}$  and the results get worse than those for  $n \leq 3$ . Although this is also seen in real space and could be ascribed to the UV-sensitive features of the higher-order SPT expansion, a more prominent feature seen in the redshift-space results suggests that the perturbative description of the redshift-space density field in Eq. (13) further

<sup>10</sup>Together with the UV-sensitive behaviors, it is also known in SPT calculations that each of the terms in loop corrections exhibits IR sensitivity, and the results are sensitive to the low- $k$  cutoff. However, summing up the contributions at each loop order, the IR-sensitive behaviors are canceled out. In Appendix F we examine this issue with the GridSPT calculations, and show that no significant IR-sensitive behaviors appear in either the real- or redshift-space power spectra.

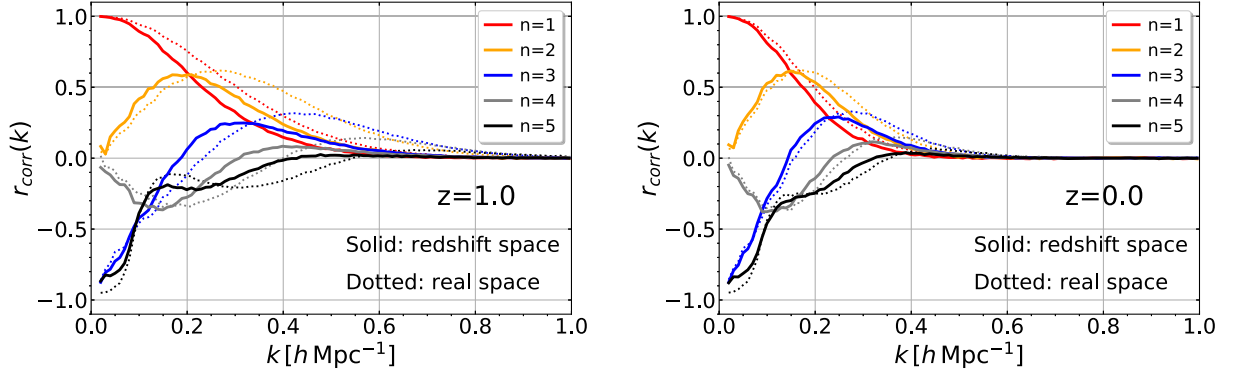


FIG. 9. Cross-correlation coefficient for GridSPT and  $N$ -body density fields,  $r_{\text{corr}}^{(n)}$ , defined in Eq. (34). Results at  $z = 1$  (left) and 0 (right) are shown. The solid and dotted lines are the results in redshift and real space, respectively.

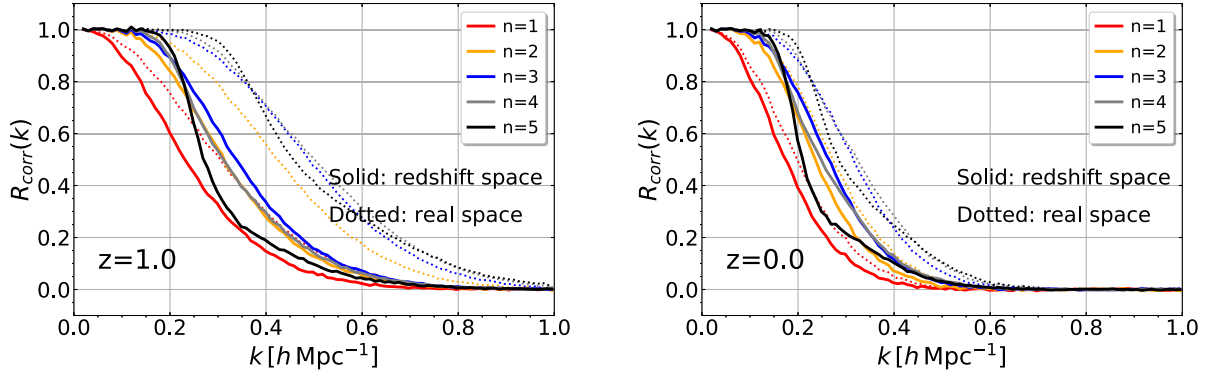


FIG. 10. Cross-correlation coefficient for GridSPT and  $N$ -body density fields,  $R_{\text{corr}}^{(n)}$ , defined in Eq. (36). The results at  $z = 1$  (left) and 0 (right) are shown in the case of real (dotted) and redshift (solid) space.

worsens the convergence of the PT expansion. Physically, in redshift space the velocity fields around and inside virialized objects are known to have a significant impact on the density fields even on large scales, referred to as the “fingers-of-God” effect [75,76]. This is partly deduced from the exact expressions given in Eq. (9) or Eq. (13), where the terms involving the line-of-sight velocity field make the density field nonperturbative. Since the SPT treatment naively Taylor expands all of the contributions, it would be difficult for calculations at finite order to capture the fingers-of-God effect, and any improvement on the PT prediction would need a nonperturbative treatment or phenomenological description (e.g., Refs. [14,18,33,77]). In the next section, we will examine one such approach, and discuss its usability by looking at the morphological and statistical properties of redshift-space density fields.

## V. PADÉ APPROXIMATION

In this section, as one of the nonperturbative resummation methods, we consider the Padé approximation and compute the *resummed* density field using the GridSPT results up to the fifth order. The Padé approximation reorganizes the original power-series expansion by

considering its rational form. Padé approximations are known to be superior to Taylor series when functions contain poles. There have been several works on the application of Padé approximations in the context of the perturbation theory of large-scale structure [50,78,79] (see also Ref. [80] for the application of the Shanks transformation). Here, we particularly focus on the redshift-space density field and apply the Padé approximations specifically to the GridSPT calculations.

Provided the PT expansion up to the  $(M + N)$ th order, Padé approximations provide a way to construct a rational expansion form involving the series expansion up to the  $M$ th and  $N$ th orders in the numerator and denominator, respectively, which we denote by Padé  $(M, N)$ :

$$\delta_{\text{SPT}}^{(S)} = \sum_{n=1}^{M+N} c_n \rightarrow \delta_{\text{Padé}}^{(S)}(\mathbf{k}) = \frac{\sum_{m=1}^M a_m}{1 + \sum_{n=1}^N b_n}, \quad (37)$$

where the coefficient  $c_n$  is given by  $c_n = \delta_n^{(S)}$ , with the quantity  $\delta_n^{(S)}$  being the Fourier-space density field computed from GridSPT based on Eqs. (15)–(19). Given the positive integers  $M$  and  $N$ , the coefficients  $a_n$  and  $b_n$  are expressed in terms of  $\{c_n\}$ . In general,  $M = N$  is the best

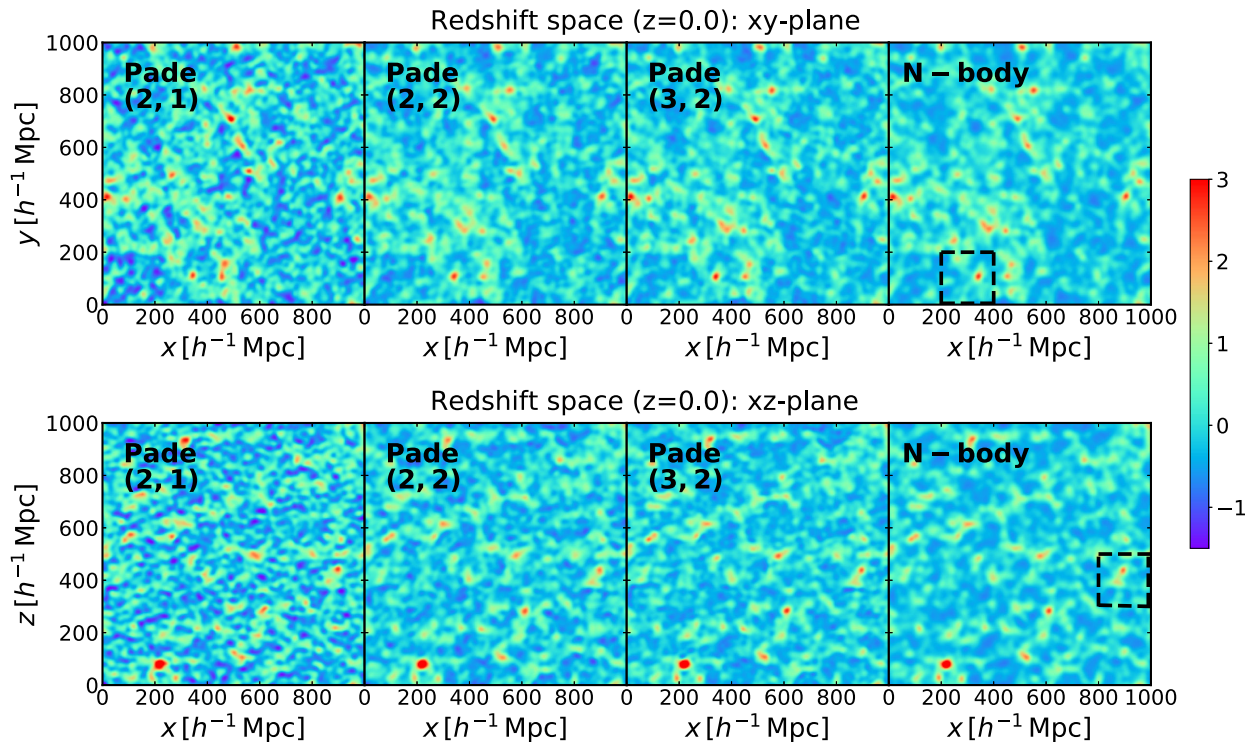


FIG. 11. 2D density field at  $z = 0$  smoothed with a Gaussian filter of  $R = 10h^{-1}$  Mpc. The redshift-space density fields obtained from Padé approximations are plotted, together with the  $N$ -body results. Similar to Figs. 1 and 2, slices of the  $x$ - $y$  (upper) and  $x$ - $z$  (lower) planes are taken, and the density fields averaged over  $10h^{-1}$  Mpc depth are shown.

choice (e.g., Ref. [81]). Here, we consider the Padé (2,1), (2,2), and (3,2), which are computed with the SPT density fields up to third, fourth, and fifth order, respectively. In Appendix D we summarize the explicit form of the coefficients  $a_n$  and  $b_n$  for each case.

In Fig. 11 the projected density fields in redshift space smoothed with a Gaussian filter of radius  $R = 10h^{-1}$  Mpc (as similarly shown in Figs. 1 and 2) are plotted. Also, in Fig. 12 we enlarge the plot of the redshift-space density fields, taken from the regions enclosed by the dashed lines in Fig. 11. These should be compared with the GridSPT results for  $n = 3, 4$ , and 5 in Figs. 1–4. We then find that the fake wobbly structures seen in the  $x$ - $z$  plane, which exhibit successive low- and high-density regions along the line of sight, fade in the resummed results with Padé approximations. As a result, the morphology and structure of density fields from the Padé (2,2) and (3,2) get much closer to the  $N$ -body results, visually regarded as an improvement.

The improvement, however, does not hold true for the statistical measures. Figure 13 shows the redshift-space power spectra at  $z = 1$  measured from a single-realization density field constructed with the Padé approximation. The resulting monopole and quadrupole spectra exhibit a rather large enhancement on small scales. This is presumably due to the UV-sensitive behaviors inherent in the SPT calculation. Unlike in the naive PT treatment that evaluates the power spectrum perturbatively from several loop corrections

[see Eqs. (25)–(28)], no cancellation of the higher-order corrections is expected in the Padé approximation. Accordingly, the measured power spectra significantly deviate from those obtained from the  $N$ -body simulations.

In Fig. 14, the cross-correlation coefficient  $R_{\text{corr}}$  is computed for the Padé approximation, and the results at  $z = 1$  (left) and 0 (right) are compared with those obtained in Sec. IV C for  $n = 3, 4$ , and 5 (dotted lines). Note again that these are obtained from the same single realization data as used in Figs. 11–13. We then find that the correlation coefficients from the Padé approximations are prone to be more suppressed than those of the naive SPT calculations. A closer look at the results of Padé (3,2) reveals that the suppression at intermediate scales around  $k \sim 0.3\text{--}0.4h$  Mpc $^{-1}$  becomes milder compared to the SPT results at  $n = 5$ , but the improvement of the cross-correlation coefficient is moderate. In all cases, the results of the Padé approximations show a rather noisy behavior, and spikes and dips are also seen in the power spectra at small scales,  $k \gtrsim 0.2h$  Mpc $^{-1}$ . Note that by applying the Padé approximation to the real-space density fields we have also seen similar noisy behavior. They are possibly caused by artificial singularities coming from the rational function in Eq. (37).<sup>11</sup> Although those singular behaviors can be apparently eliminated by applying the smoothing function

<sup>11</sup>In evaluating Eq. (37) numerically, we added a small positive number to the denominator to prevent divergence.

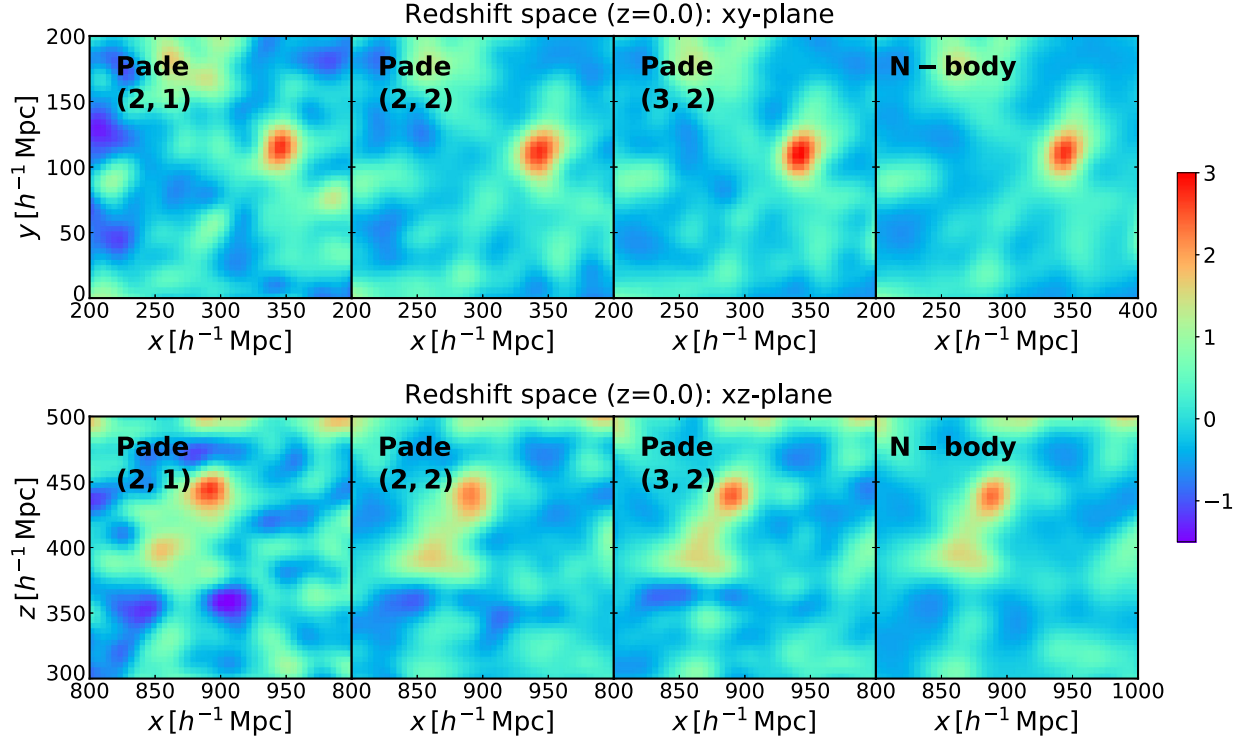


FIG. 12. Same as Fig. 11, but an enlarged plot of the 2D density field over  $200 \times 200 h^{-1}$  Mpc size is shown for the region enclosed by the dashed line in the right panels of Fig. 11.

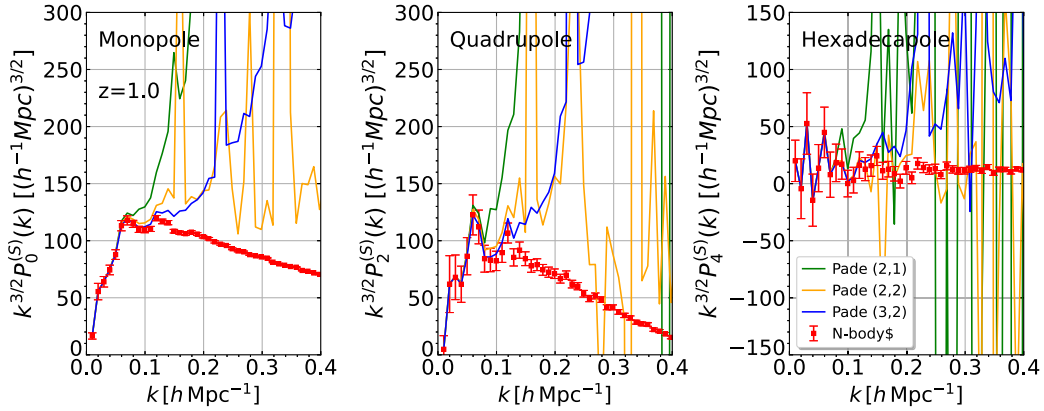


FIG. 13. Redshift-space power spectrum at  $z = 1$ , obtained from the Padé approximations of GridSPT calculations. Green, yellow, and blue solid lines are the power spectra computed with the Padé (2,1), (2,2), and (3,2), respectively. These are compared with  $N$ -body simulations (filled squares), which are taken from Fig. 5.

and hence we do not see such a spiky structure in Figs. 11 and 12, these could severely affect the statistical quantities measured from the unfiltered density fields. Since the singular points eventually appear in the regions where the higher-order density fields receive a large correction, the application of the Padé approximation may not be generally suited to improving the convergence of the SPT

expansion at the field level. We conclude that simply rewriting the SPT expansion in a rational form does not improve the predictions in redshift space. Rather, mitigating the UV sensitivity in the SPT calculations would be essential, and implementing a regularization scheme including the effective-field-theory treatment would be thus important.

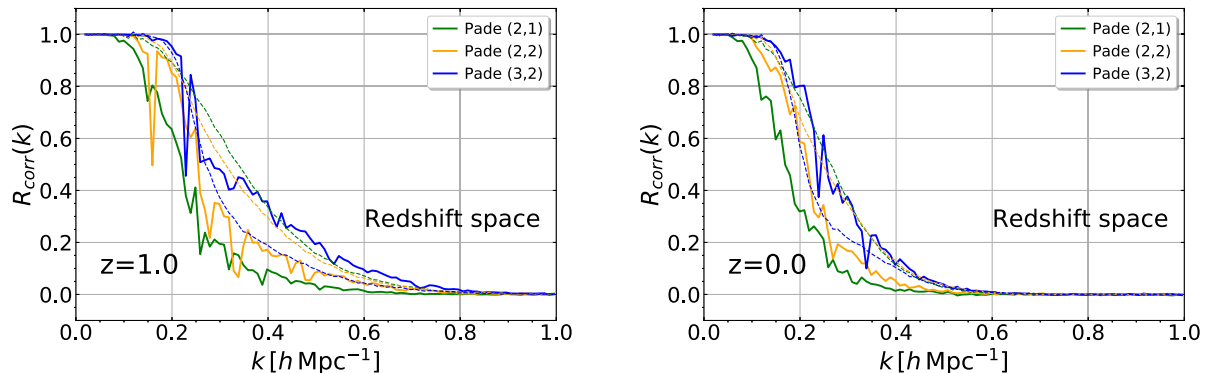


FIG. 14. Cross-correlation coefficient for density fields obtained from the Padé approximations of the GridSPT calculations and  $N$ -body simulations (solid lines). The results in redshift space are presented at  $z = 1$  (left) and  $0$  (right). The dashed lines show the GridSPT results at third, fourth, and fifth order, which are the same as the solid lines in Fig. 10.

## VI. CONCLUSION AND DISCUSSIONS

In this paper, we have extended our previous works on a grid-based SPT algorithm—GridSPT—to implement RSDs on grids. The key expression is given in Eq. (13), in which the redshift-space density field is expressed in terms of the real-space quantities (density and velocity fields) given at a redshift-space position. Thus, this expression allows us to apply the real-space results of GridSPT calculations directly for a perturbative evaluation of the redshift-space density field on grids. With this new implementation, we have demonstrated the GridSPT calculations in redshift space up to the fifth order, and investigated the morphological and statistical properties of the SPT density fields, which we have also compared with cosmological  $N$ -body simulations.

We found that the redshift-space power spectrum and bispectrum obtained from the GridSPT calculations agree well with analytical SPT results up to the two-loop and one-loop order, respectively. Note that the two-loop SPT power spectra were numerically evaluated and presented for the first time in this paper. In redshift space, adding the higher-loop corrections is shown to significantly change the amplitudes of both the power spectrum and bispectrum. In particular, we found that the power spectrum sensitively depends on the small-scale cutoff. This implies that the convergence of the SPT expansion [Eq. (13)] in redshift space becomes worse than that in real space due to the higher-derivative operators  $\tilde{\nabla}_z^n$ . In fact, comparing the generated density fields from the GridSPT calculations with those obtained from the  $N$ -body simulations, we see that the SPT expansion is prone to producing fake structures in redshift space, and even at large scales, unphysical wobbly structures appear along the line of sight. Accordingly, the statistical correlation of the GridSPT density field with  $N$ -body results is rather poor, and as we go to higher  $k$ , the resultant cross correlation becomes suppressed more rapidly than that in real space.

To remedy the poor convergence of the SPT expansion in redshift space, we have considered the Padé approximation,

and applied it to the Fourier-space density fields. Rewriting the SPT expansion with a rational expansion form, the morphological properties of the smoothed density fields get visually better, and the wobbly structures mostly disappear. However, the resultant power spectra exhibit a large enhancement together with spikes and dips at small scales, which are also seen in the cross-correlation coefficients. These presumably originate from the UV-sensitive behaviors inherent in the SPT calculation, and higher-order density fields get a rather large correction at small scales. With the expansion reorganized in a rational form, no cancellation of UV sensitivity terms occurs, leading eventually to the singularities. We thus conclude that simply reorganizing the SPT expansion does not improve the predictions, and mitigating the UV sensitivity would be rather crucial.

Finally, as we mentioned in Sec. I, the implementation of the RSD effect in GridSPT is not our final goal, but rather an important and necessary step toward a practical application of the method to observations. In Ref. [29] we demonstrated that the grid-based algorithm for SPT calculations allows us to easily incorporate the observational systematics, such as the survey window function and masks. In addition, it is rather straightforward to implement a general expansion scheme to deal with the galaxy bias that has been actually exploited on the basis of SPT (e.g., Refs. [21,22,82–85]; see Ref. [1] for review). With an effective-field-theory treatment at the field level, we anticipate that the UV-sensitive behaviors can be mitigated, and by incorporating further the IR resummation technique (which can handle the large-scale bulk flow) into the GridSPT, an efficient and stable PT prediction would become possible in redshift space. Consistently incorporating all observational effects to the grid-based theoretical calculations may provide an efficient framework to maximize the cosmological information obtained from the galaxy survey data (e.g., Refs. [86–88]). An investigation

along this direction is important for future practical application, and we will continue to work on these.

### ACKNOWLEDGMENTS

A. T. thanks Satoshi Tanaka for his comments and discussion on the higher-order differential scheme, and Takahiko Matsubara for his suggestions on the Padé approximation. This work was supported in part by MEXT/JSPS KAKENHI Grants No. JP17H06359 (A. T.), No. JP17K14273, No. JP19H00677 (T. N.), No. JP20H05861 and No. JP21H01081 (A. T. and T. N.). We also acknowledge financial support from Japan Science and Technology Agency (JST) AIP Acceleration Research Grant No. JP20317829 (A. T. and T. N.). D. J. acknowledges support from NASA 80NSSC18K1103. Numerical computations were partly carried out at the Yukawa Institute Computer Facility.

### APPENDIX A: ON THE ALIASING CORRECTION IN GridSPT CALCULATIONS

In this appendix, we discuss the dealiasing treatment to mitigate the spurious high-frequency modes arising from the nonlinear calculations of fields on grids. After describing dealiasing methods in Appendix A 1, we compare the

results of GridSPT calculations between several dealiasing treatments in Appendix A 2.

#### 1. Aliasing corrections

Let us first recall how the aliasing effect affects the GridSPT calculations. For simplicity, we consider a one-dimensional grid space with a side length of  $L$ , and compute the product of the two fields  $A_1(x)$  and  $A_2(x)$ , where the position  $x$  is defined over the range  $0 \leq x \leq L$ . For a grid number  $N$ , the discrete Fourier transform of the fields  $A_k$  is described by

$$A_k(x_j) = \sum_{n=-N/2}^{N/2-1} A_k(k_n) e^{ik_n x_j}, \quad (k = 1, 2), \quad (\text{A1})$$

where the discrete Fourier mode  $k_n$  is given by  $k_n = 2n\pi/L$ , and the position in grid space,  $x_j$ , is discretized as  $x_j = (j/N)L$  for  $j = 0, \dots, N-1$ . In GridSPT the product of the two fields  $A_1$  and  $A_2$  is computed in configuration space, and then the derivative operations are applied in Fourier space. Using Eq. (A1), the Fourier coefficient of the product  $A_1(x)A_2(x)$  for the mode  $k_n$  becomes

$$\frac{1}{N} \sum_{j=-N/2}^{N/2-1} A_1(x_j)A_2(x_j)e^{-ik_n x_j} = \sum_{\ell, m=-N/2}^{N/2-1} \delta_{\ell+m, n}^K A_1(k_\ell)A_2(k_m) + \sum_{\ell, m=-N/2}^{N/2-1} \delta_{\ell+m, n \pm N}^K A_1(k_\ell)A_2(k_m), \quad (\text{A2})$$

where we used the fact that

$$\frac{1}{N} \sum_{j=0}^{N-1} e^{ipx_j} = \begin{cases} 1 & (p = \frac{2\pi}{L}Nm, \quad m = 0, \pm 1, \pm 2, \dots), \\ 0 & \text{otherwise.} \end{cases} \quad (\text{A3})$$

In Eq. (A2), the first term on the right-hand side represents the contribution that we want to calculate. On the other hand, the second term is the aliasing contribution originating from the discreteness of the grid space. To simple way to eliminate these spurious contributions is to discard the high-frequency modes that can produce the aliasing effect. To be precise, if we set the fields  $A_1(k_n)$  and  $A_2(k_n)$  to zero for  $|n| > N/3$ , the nonvanishing modes in Eq. (A2) are restricted to  $|\ell + m - n| < N$ , and thus the aliasing contribution does not appear. Since the mode  $k_n$  at  $|n| = N/3$  corresponds to  $2/3$  times the Nyquist frequency, this zero-padding method is called the  $2/3$  rule [89]. Note that the prescription given here can be generalized to the case for higher-order products. That is, in order to avoid the aliasing effect for a product of  $M$  fields,  $\Pi_{k=1}^M A_k(x_j)$ , the modes of the fields  $A_k(k_n)$  for  $|n| > N/(M+1)$  should be set to zero, corresponding to modes larger than  $2/(M+1)$  times the Nyquist frequency.

Further generalizing the above discussion to three-dimensional grid space, Refs. [26,29] adopted an isotropic low-pass filter (called sharp- $k$ ) with the critical wave number  $k_{\text{crit}} = (2/3)k_{\text{Nyq}}$ , by which the Fourier modes in  $|\mathbf{k}| > k_{\text{crit}}$  are set to zero. The filter is applied at each step when we proceed to higher-order GridSPT calculations. Then, the generated PT fields up to the fifth order reproduce the desired properties known in the analytical calculations. However, the procedure used in previous works is not a unique choice. Instead of using an isotropic filter, we may introduce an anisotropic filter in which the zero padding is applied to the modes having  $|k_{x,y,z}| > k_{\text{crit}}$ . This also eliminates the spurious aliasing contributions. Furthermore, recalling that the  $n$ th-order PT fields are expressed as the  $n$ th-order product of the linear density fields, an alternative method of aliasing correction for the GridSPT calculation at  $n$ th order is to adopt the  $2/(n+1)$  rule only once. That is, the low-pass filter with  $k_{\text{crit}} = 2/(n+1)k_{\text{Nyq}}$  is applied only to the (initial) linear density field, and the subsequent higher-order PT calculations are performed up to  $n$ th order, without taking any filter.

## 2. Comparison of dealiasing treatments

Let us quantitatively study the possible impact of the dealiasing treatment on the GridSPT calculations, focusing on the statistical quantities obtained from the density fields up to the fifth order in real and redshift space.

Based on the discussions in Appendix A 1, dealiasing prescriptions we here examine are summarized as follows:

- (1) 2/3 rule (iso): An isotropic sharp- $k$  filter with  $k_{\text{crit}} = (2/3)k_{\text{Nyq}}$  is applied to the PT fields at every order of PT calculations.
- (2) 2/3 rule (aniso): An anisotropic sharp- $k$  filter with  $k_{\text{crit}} = (2/3)k_{\text{Nyq}}$ , by which the modes having  $|k_{x,y,z}| > k_{\text{crit}}$  are set to zero, is applied to the PT fields at every order of PT calculations.
- (3) 1/3-rule (iso): An isotropic sharp- $k$  filter with  $k_{\text{crit}} = (1/3)k_{\text{Nyq}}$  is applied only to the initial density fields before PT calculations.
- (4) 1/3-rule (aniso): An anisotropic sharp- $k$  filter with  $k_{\text{crit}} = (1/3)k_{\text{Nyq}}$ , by which the modes having  $|k_{x,y,z}| > k_{\text{crit}}$  are set to zero, is applied only to the initial density fields before PT calculations.

In Figs. 15 and 16, using the above dealiasing treatments, GridSPT results of the power spectra and bispectra are shown at  $z = 1$ , adopting the number of grids  $N_{\text{grid}} = 1200^3$  and  $600^3$  in the upper and lower panels, respectively. Here, the power spectra computed with GridSPT are at two-loop order, while the bispectra are at one-loop order. Both results are obtained from the same initial seed as used in the

$N$ -body simulation, whose results are also depicted as filled circles for reference. For single realization data, the number of available Fourier modes is limited at large scales, and the measured results from the  $N$ -body simulation suffer from the effect of finite-mode sampling, which is known to be significant for low- $k$  modes [90]. Hence, to make a fair comparison, we add corrections due to the finite-mode sampling to the GridSPT results. That is, contributions with odd powers of the (Gaussian) linear density field,  $(P_{12}, P_{23}, P_{14})$  and  $(B_{111}, B_{113}, B_{122})$ , are added to the power spectrum and bispectrum, respectively [see Eqs. (32) and (33) for definitions of  $P_{ab}$  and  $B_{abc}$ ]. Although the odd-power contributions usually vanish in the limit of an infinite number of Fourier modes, these contributions do exist in the  $N$ -body realization. Indeed, taking them into account in the GridSPT calculations makes the agreement with  $N$ -body results better, especially at  $k \lesssim 0.1 h \text{ Mpc}^{-1}$ .

In Fig. 15, apart from a bumpy scale-dependent feature at  $k \gtrsim 0.2 h \text{ Mpc}^{-1}$ , a prominent difference arising from the dealiasing treatments appears if we adopt a smaller number of grids,  $N_{\text{grid}} = 600$  (lower). Typically, the impact gets large for the redshift-space monopole and quadrupole spectra, and adopting the anisotropic sharp- $k$  filter tends to suppress the power spectrum amplitude compared to the isotropic counterpart. Applying the 1/3 rule to only the initial condition also suppresses the power, compared to the 2/3 rule at every PT order. These behaviors originate from the change of the mode transfer due to different cutoff

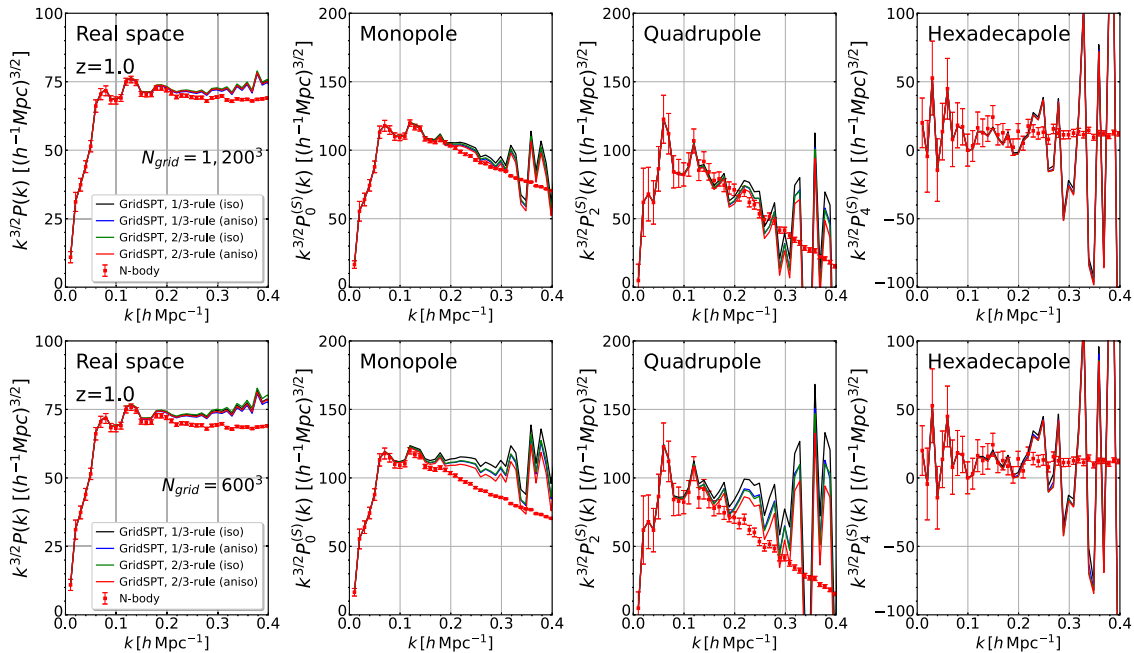


FIG. 15. Impact of the dealiasing treatments on the real- and redshift-space power spectra at two-loop order in GridSPT calculations (solid lines). The results at  $z = 1$  are shown, multiplied by  $k^{3/2}$ . The upper and lower panels represent the GridSPT results when adopting the number of grids  $N_{\text{grid}} = 1200^3$  and  $600^3$ , respectively. For reference,  $N$ -body results are also shown in each panel (red crosses), with error bars indicating the sampling noise estimated from the number of Fourier modes in each bin.

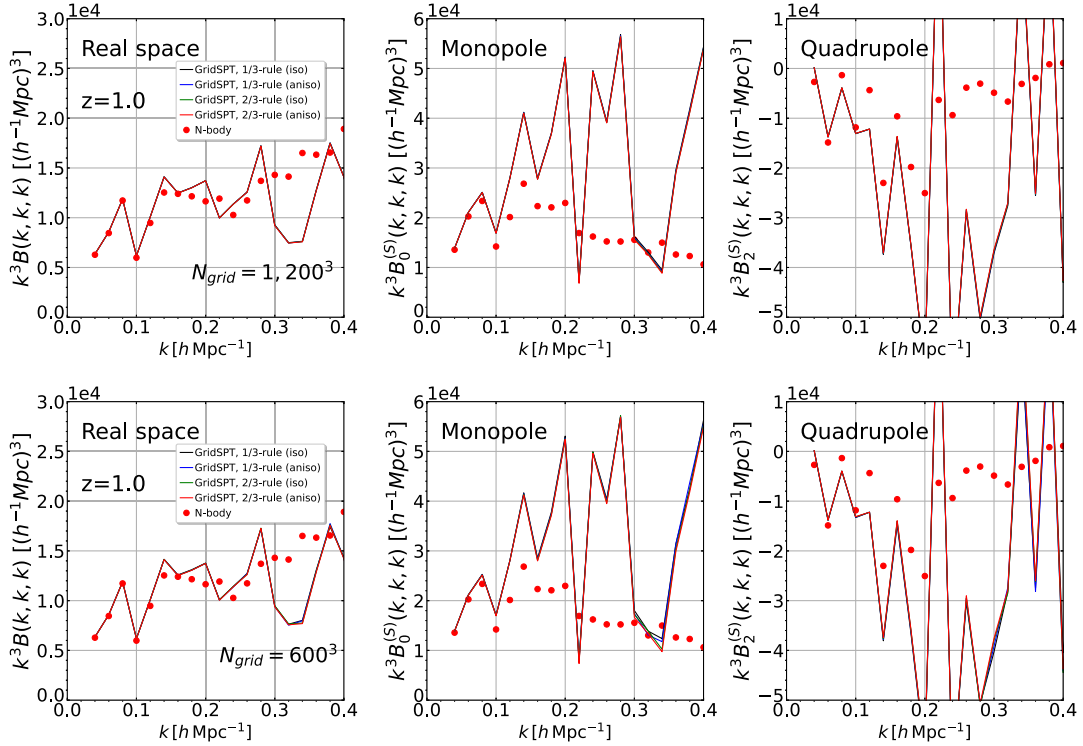


FIG. 16. Same as Fig. 15, but for the GridSPT results of the one-loop bispectrum in an equilateral configuration, multiplied by  $k^3$ . The upper and lower panels plot the GridSPT results when adopting the number of grids  $N_{\text{grid}} = 1200^3$  and  $600^3$ , together with the measured results from  $N$ -body simulations (red crosses).

strategies and the cutoff scales imposed, leading to a visible change in the power spectrum amplitude. The effect would become more significant at lower redshifts. On the other hand, looking at the one-loop bispectrum shown in Fig. 16, we hardly see a clear difference.

Based on the discussion and the results in Figs. 15 and 16, in the main text we adopt the 1/3 rule for the dealiasing treatment, since it is considered to have little effect on the mode-coupling structure. Using a simple isotropic sharp- $k$  filter, the GridSPT calculation is performed mainly with  $N_{\text{grid}} = 1200^3$ , and the results are presented in Sec. IV.

## APPENDIX B: ANALYTICAL EXPRESSIONS FOR SPT POWER SPECTRUM AND BISPECTRUM IN REDSHIFT SPACE

In this appendix, we present the analytical expressions of the SPT power spectrum and bispectrum in redshift space.

Let us first recall that in the SPT treatment, the redshift-space density field  $\delta^{(S)}$  is expanded in powers of the linear density field  $\delta_1$  [see Eq. (7)], and in Fourier space we have

$$\delta^{(S)}(\mathbf{k}) = \sum_{n=1} \int \frac{d^3\mathbf{p}_1 \cdots d^3\mathbf{p}_n}{(2\pi)^{3n}} \delta_D(\mathbf{k} - \mathbf{p}_{1\dots n}) \times Z_n(\mathbf{p}_1, \dots, \mathbf{p}_n) \delta_1(\mathbf{p}_1) \cdots \delta_1(\mathbf{p}_n), \quad (\text{B1})$$

with the wave vector  $\mathbf{p}_{1\dots n}$  defined by  $\mathbf{p}_{1\dots n} \equiv \mathbf{p}_1 + \cdots + \mathbf{p}_n$ . Here, the kernels  $Z_n$  characterize the mode coupling in redshift space between Fourier modes, and they are symmetric with respect to the exchange of their arguments. These kernels are analytically constructed, and are expressed in terms of the real-space PT kernels,  $F_n$  and  $G_n$ , for the  $n$ th-order density and velocity-divergence fields, given by

$$\delta_n(\mathbf{k}) = \int \frac{d^3\mathbf{p} \cdots d^3\mathbf{p}_1}{(2\pi)^{3n}} \delta_D(\mathbf{k} - \mathbf{p}_{1\dots n}) \times F_n(\mathbf{p}_1, \dots, \mathbf{p}_n) \delta_1(\mathbf{p}_1) \cdots \delta_1(\mathbf{p}_n), \quad (\text{B2})$$

$$\theta_n(\mathbf{k}) = \sum_{n=1} \int \frac{d^3\mathbf{p} \cdots d^3\mathbf{p}_1}{(2\pi)^{3n}} \delta_D(\mathbf{k} - \mathbf{p}_{1\dots n}) \times G_n(\mathbf{p}_1, \dots, \mathbf{p}_n) \delta_1(\mathbf{p}_1) \cdots \delta_1(\mathbf{p}_n), \quad (\text{B3})$$

with  $F_1 = 1 = G_1$ . The explicit forms of these kernels are constructed through a recurrence relation (see, e.g., Refs. [25,91,92]), which corresponds to the Fourier transform of the formula given by Eq. (6). Using the expressions in Eqs. (B2) and (B3), the expansion form of  $\delta^{(S)}$ , given in Eq. (11), is reorganized with respect to powers of  $\delta_1$ , leading to the form given by Eq. (B1), from which we can read off the analytical expressions for the kernel  $Z_n$

recursively. In the last step, the kernel  $Z_n$  has to be symmetrized by summing up the expressions with all possible permutations of their arguments. The explicit forms of  $Z_n$  can be found in the literature (e.g., Refs. [61,93] up to third and fourth order, respectively). Note that the kernel  $Z_n$  includes the terms with an explicit dependence on the linear growth factor  $f$ , and by setting  $f$  to zero, it is reduced to the real-space PT kernel  $F_n$ .

Provided the kernel  $Z_n$ , the analytical expressions for the redshift-space power spectrum and bispectrum are derived based on the definitions in Sec. IV B. The SPT power spectrum at two-loop order, given in Eq. (25), consists of the six contributions summarized in Eqs. (26)–(28). With the help of the Wick theorem, their analytical expressions are obtained from Eq. (32):

$$P_{11}^{(S)}(\mathbf{k}) = \{Z_1(\mathbf{k})\}^2 P_L(k), \quad (\text{B4})$$

$$P_{13}^{(S)}(\mathbf{k}) = 3Z_1(\mathbf{k})P_L \int \frac{d^3\mathbf{p}}{(2\pi)^3} Z_3(\mathbf{p}, -\mathbf{p}, \mathbf{k})P_L(p), \quad (\text{B5})$$

$$P_{22}^{(S)}(\mathbf{k}) = 2 \int \frac{d^3\mathbf{p}}{(2\pi)^3} \{Z_2(\mathbf{p}, \mathbf{k} - \mathbf{p})\}^2 P_L(p)P_L(|\mathbf{k} - \mathbf{p}|), \quad (\text{B6})$$

$$P_{15}^{(S)}(\mathbf{k}) = 15Z_1(\mathbf{k})P_L(k) \times \int \frac{d^3\mathbf{p}d^3\mathbf{q}}{(2\pi)^6} \{Z_5(\mathbf{p}, \mathbf{q}, -\mathbf{p}, -\mathbf{q}, \mathbf{k})\} P_L(p)P_L(q), \quad (\text{B7})$$

$$P_{24}^{(S)}(\mathbf{k}) = 12 \int \frac{d^3\mathbf{p}d^3\mathbf{q}}{(2\pi)^6} Z_2(\mathbf{p}, \mathbf{k} - \mathbf{p}) \times Z_4(\mathbf{p}, \mathbf{q}, -\mathbf{q}, \mathbf{k} - \mathbf{p})P_L(p)P_L(q)P_L(|\mathbf{k} - \mathbf{p}|), \quad (\text{B8})$$

$$P_{33}^{(S)}(\mathbf{k}) = 9Z_1(\mathbf{k})P_L(k) \left\{ \int \frac{d^3\mathbf{p}}{(2\pi)^3} Z_3(\mathbf{p}, -\mathbf{p}, \mathbf{k})P_L(p) \right\}^2 + 6 \int \frac{d^3\mathbf{p}d^3\mathbf{q}}{(2\pi)^6} \{Z_3(\mathbf{p}, \mathbf{q}, \mathbf{k} - \mathbf{p} - \mathbf{q})\}^2 \times P_L(p)P_L(q)P_L(|\mathbf{k} - \mathbf{p} - \mathbf{q}|), \quad (\text{B9})$$

where the function  $P_L$  is the linear power spectrum in real space, i.e.,  $P_L = P_{11}$ . On the other hand, the SPT bispectrum at one-loop order has four terms, as given in Eqs. (30) and (31). From Eq. (33), these are analytically expressed as follows:

$$B_{112}^{(S)}(\mathbf{k}_1, \mathbf{k}_2, \mathbf{k}_3) = 2Z_2(\mathbf{k}_1, \mathbf{k}_2)Z_1(\mathbf{k}_1)Z_1(\mathbf{k}_2) \times P_L(k_1)P_L(k_2), \quad (\text{B10})$$

$$B_{123}^{(S)}(\mathbf{k}_1, \mathbf{k}_2, \mathbf{k}_3) = 6Z_1(\mathbf{k}_1)P_L(k_1) \int \frac{d^3\mathbf{p}}{(2\pi)^3} Z_2(\mathbf{p}, \mathbf{k}_2 - \mathbf{p}) \times Z_3(-\mathbf{k}_1, -\mathbf{p}, -\mathbf{k}_2 + \mathbf{p}) \times P_L(p)P_L(|\mathbf{k}_2 - \mathbf{p}|) + 6Z_1(\mathbf{k}_1)Z_2(\mathbf{k}_1, \mathbf{k}_2)P_L(k_1)P_L(k_2) \times \int \frac{d^3\mathbf{p}}{(2\pi)^3} Z_3(\mathbf{k}_2, \mathbf{p}, -\mathbf{p})P_L(p), \quad (\text{B11})$$

$$B_{114}^{(S)}(\mathbf{k}_1, \mathbf{k}_2, \mathbf{k}_3) = 12Z_1(\mathbf{k}_1)Z_1(\mathbf{k}_2)P_L(k_1)P_L(k_2) \times \int \frac{d^3\mathbf{p}}{(2\pi)^3} Z_4(-\mathbf{k}_1, -\mathbf{k}_2, \mathbf{p}, -\mathbf{p})P_L(p), \quad (\text{B12})$$

$$B_{222}^{(S)}(\mathbf{k}_1, \mathbf{k}_2, \mathbf{k}_3) = 8 \int \frac{d^3\mathbf{p}}{(2\pi)^3} Z_2(\mathbf{k}_1 - \mathbf{p}, \mathbf{p}) \times Z_2(\mathbf{k}_2 + \mathbf{p}, -\mathbf{p})Z_2(-\mathbf{k}_2 - \mathbf{p}, -\mathbf{k}_1 + \mathbf{p}) \times P_{11}(|\mathbf{k}_1 - \mathbf{p}|)P_L(p)P_L(|\mathbf{k}_2 + \mathbf{p}|). \quad (\text{B13})$$

Finally, we note that the analytical SPT results presented in this paper are the multipole moments of the power spectrum and bispectrum. Thus, on top of the loop integrals shown above, one also has to evaluate the integrals over the angles [see Eqs. (21) and (22)]. As a result, the six- and five-dimensional integrals have to be evaluated for the power spectrum and bispectrum, respectively.<sup>12</sup> In order to deal with these multidimensional integrals, we adopt a Monte Carlo integration technique, specifically using the quasirandom sampling in the CUBA library [94] to directly compute them.

### APPENDIX C: UV SENSITIVITY OF SPT CALCULATIONS IN REDSHIFT SPACE

In this appendix, we discuss the UV sensitivity of the SPT calculations and examine the cutoff dependence of the predicted power spectra and bispectra.

In SPT, higher-order PT corrections generally involve multidimensional loop integrals, and the support of their integrands gets wider for higher-loop integrals (e.g., Refs. [50,51]). That is, as we go to higher orders, the result of the loop corrections becomes more sensitive to the cutoff of the integral. While the Galilean invariance of the SPT calculations ensures the cancellation of the IR divergence and hence the IR sensitivity can become ignorable for a sufficiently small cutoff wave number (see Appendix F for

<sup>12</sup>In the power spectrum case, one can use the rotational symmetry with respect to the line-of-sight direction to partly reduce the loop integrals.

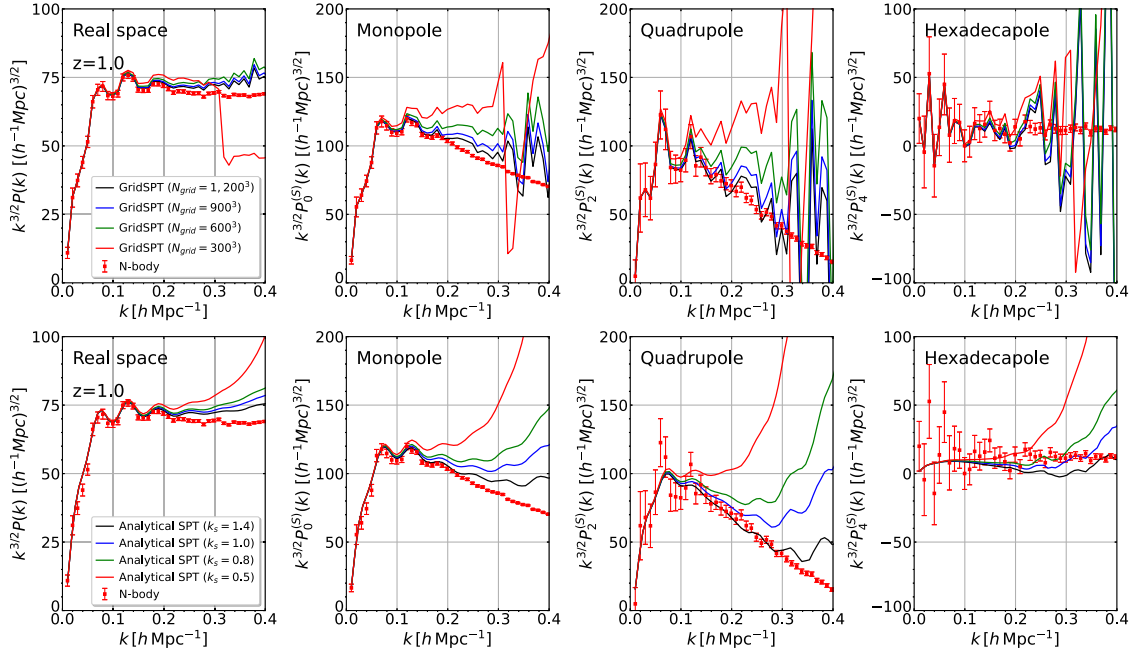


FIG. 17. Sensitivity of the power spectrum predictions to the high- $k$  cutoff in real and redshift space. The results at  $z = 1$  are plotted, multiplied by  $k^{3/2}$ . In the upper panels, varying the number of grids  $N_{\text{grid}}$ , the GridSPT results of the two-loop power spectra at  $z = 1$  are shown (solid). In all cases, the box size of the GridSPT calculations is held fixed at  $L_{\text{box}} = 1000h^{-1}$  Mpc. On the other hand, the lower panels show the analytical SPT predictions when varying the high- $k$  cutoff in the linear power spectrum. Again, in all cases the low- $k$  cutoff in the linear spectrum is set to  $k_{\text{min}} = 2\pi/L_{\text{box}} \simeq 6.28 \times 10^{-3} h \text{ Mpc}^{-1}$ . For reference, the  $N$ -body results are also shown in each panel (red crosses).

an explicit demonstration), such a cancellation does not occur for the UV-sensitive behaviors, and care must be taken when choosing the UV cutoff (see, e.g., Refs. [71,95] for an explicit demonstration).

In Figs. 17 and 18 we plot the SPT predictions of two-loop power spectra and one-loop bispectra at  $z = 1$ , respectively. In each case, the upper panels show the GridSPT results when varying the number of grids  $N_{\text{grid}}$  and fixing the box size to  $L_{\text{box}} = 1000h^{-1}$  Mpc. On the other hand, the lower panels show the analytical SPT predictions when varying the high- $k$  cutoff in the linear power spectrum. In all analytical SPT results, the low- $k$  cutoff of  $k_{\text{min}} = 2\pi/L_{\text{box}} \simeq 6.28 \times 10^{-3} h \text{ Mpc}^{-1}$  is adopted. The high- $k$  cutoff scales in the analytical SPT results are taken to be slightly larger than the dealiasing filter scales ( $k_{\text{crit}} = k_{\text{Nyq}}/3$ ) for the GridSPT calculations,<sup>13</sup> but we find a reasonable agreement between the two predictions.

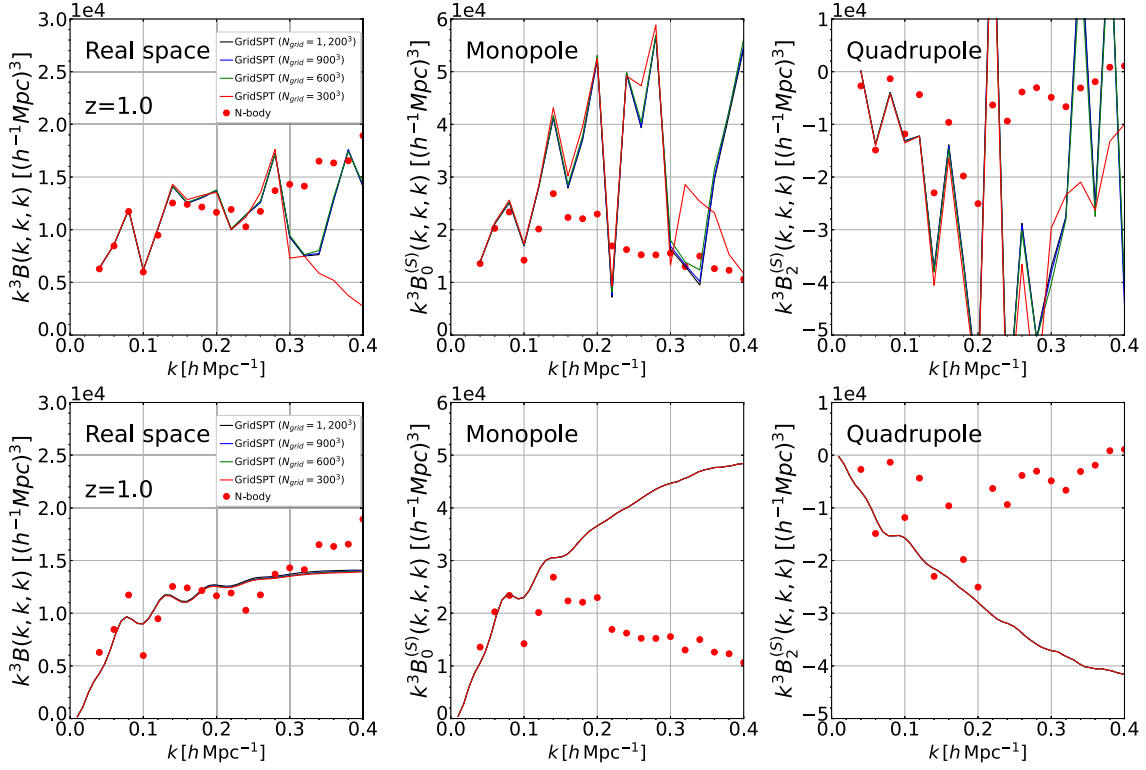
In Fig. 17, we see that decreasing the high- $k$  cutoff or the number of grids enhances the power spectrum on small scales. While these trends have been known in real space (e.g., Refs. [71,95]), a notable point is that the redshift-space power spectra exhibit a strong scale-dependent enhancement, not only in GridSPT but also in analytical SPT

calculations. In real space, when we increase the cutoff scale or number of grids, the predicted amplitude of the power spectrum tends to converge. In redshift space, however, we still see a sizable change in the amplitude, especially at  $k \gtrsim 0.3h \text{ Mpc}^{-1}$ , indicating that the UV sensitivity is more serious in redshift space. This is perhaps due to the increasing number of PT corrections at higher order, arising from the line-of-sight velocity contributions [see Eq. (13)]. Thus, in redshift space, a careful choice of high- $k$  cutoff is necessary for the two-loop SPT predictions of the power spectrum.

On the other hand, the one-loop predictions of the bispectrum, shown in Fig. 18, do not have a strong UV sensitivity in both real and redshift space, and the analytical SPT and GridSPT results with different high- $k$  cutoffs or numbers of grids  $N_{\text{grid}}$  almost coincide with each other. These trends are qualitatively similar to those in the one-loop power spectrum, for which we checked that they are indeed insensitive to the high- $k$  cutoff.

To sum up, the cutoff dependence of the SPT prediction is significant in the power spectrum calculation at two-loop order, and in redshift space, even with a large UV cutoff, the convergence of the power spectrum result seems to be slow. Thus, the GridSPT prediction in redshift space suffers from a rather strong UV sensitivity. However, this is indeed consistent with the analytical SPT calculations, and as long as we consider the PT calculations at fifth order, this is only the case for the power spectrum.

<sup>13</sup>For reference, the dealiasing filter scales shown in the upper panels are estimated as follows:  $k_{\text{crit}} = 1.26h \text{ Mpc}^{-1}$  (black,  $N_{\text{grid}} = 1200^3$ ),  $0.94h \text{ Mpc}^{-1}$  (blue,  $N_{\text{grid}} = 900^3$ ),  $0.63h \text{ Mpc}^{-1}$  (green,  $N_{\text{grid}} = 600^3$ ), and  $0.31h \text{ Mpc}^{-1}$  (red,  $N_{\text{grid}} = 300^3$ ).


 FIG. 18. Same as Fig. 17, but for the results of the one-loop bispectra spectra at  $z = 1$ , multiplied by  $k^3$ .

#### APPENDIX D: COEFFICIENTS OF PADÉ APPROXIMATIONS

In this appendix, we present the explicit form of the coefficients  $a_n$  and  $b_n$  for the density fields  $\delta_{\text{Padé}}^{(S)}$  given in Eq. (37), which are expressed in terms of the redshift-space SPT density fields,  $\delta_n^{(S)}$ .

To derive the explicit expressions, we first introduce a bookkeeping parameter  $\epsilon$ , and rewrite the coefficients as  $a_n \rightarrow \epsilon^n a_n$ ,  $b_n \rightarrow \epsilon^n b_n$ , and  $c_n \rightarrow \epsilon^n a_c$ . We then equate the SPT density field up to  $(M+N)$ th order to the rational form of Padé  $(M, N)$ ,  $\delta_{\text{Padé}}^{(S)}$ , given in Eq. (37). We have

$$\left\{ 1 + \sum_{n=1}^N \epsilon^n b_n \right\} \sum_{n=1}^{M+N} \epsilon^n c_n = \sum_{m=1}^M \epsilon^m a_m. \quad (\text{D1})$$

Organizing the above expression in terms of powers of expansion parameter  $\epsilon$ , the order-by-order comparison between both sides yields the equations for  $a_n$  and  $b_n$ , involving also the coefficient  $c_n$ . Solving these equations for a given set of numbers  $(M, N)$ , the coefficients  $a_n$  and  $b_n$  are determined uniquely, and are expressed in terms of  $c_n$ . Recalling that  $c_n$  is written as  $c_n = \delta_n^{(S)}$ , we obtain the explicit expressions for the coefficients  $a_n$  and  $b_n$  as follows:

##### Padé (2,1)

$$a_1 = \delta_1^{(S)}, \quad (\text{D2})$$

$$a_2 = \frac{\{\delta_2^{(S)}\}^2 - \delta_1^{(S)} \delta_3^{(S)}}{\delta_2^{(S)}}, \quad (\text{D3})$$

$$b_1 = -\frac{\delta_3^{(S)}}{\delta_2^{(S)}}. \quad (\text{D4})$$

##### Padé (2,2)

$$a_1 = \delta_1^{(S)}, \quad (\text{D5})$$

$$a_2 = \frac{\{\delta_2^{(S)}\}^3 - 2\delta_1^{(S)} \delta_2^{(S)} \delta_3^{(S)} + \{\delta_1^{(S)}\}^2 \delta_4^{(S)}}{\{\delta_2^{(S)}\}^2 - \delta_1^{(S)} \delta_3^{(S)}}, \quad (\text{D6})$$

$$b_1 = \frac{\delta_1^{(S)} \delta_4^{(S)} - \delta_2^{(S)} \delta_3^{(S)}}{\{\delta_2^{(S)}\}^2 - \delta_1^{(S)} \delta_3^{(S)}}, \quad (\text{D7})$$

$$b_2 = \frac{\{\delta_3^{(S)}\}^2 - \delta_2^{(S)} \delta_4^{(S)}}{\{\delta_2^{(S)}\}^2 - \delta_1^{(S)} \delta_3^{(S)}}. \quad (\text{D8})$$

Padé (3,2)

$$a_1 = \delta_1^{(S)}, \quad (\text{D9})$$

$$a_2 = \frac{\delta_2^{(S)}[\{\delta_3^{(S)}\}^2 - \delta_2^{(S)}\delta_4^{(S)}] - \delta_1^{(S)}\{\delta_3^{(S)}\delta_4^{(S)} - \delta_2^{(S)}\delta_5^{(S)}\}}{\{\delta_3^{(S)}\}^2 - \delta_2^{(S)}\delta_4^{(S)}}, \quad (\text{D10})$$

$$a_3 = \frac{\delta_3^{(S)}[\{\delta_3^{(S)}\}^2 - 2\delta_2^{(S)}\delta_4^{(S)} - \delta_1^{(S)}\delta_5^{(S)}] + \delta_1^{(S)}\{\delta_4^{(S)}\}^2 + \{\delta_2^{(S)}\}^2\delta_5^{(S)}}{\{\delta_3^{(S)}\}^2 - \delta_2^{(S)}\delta_4^{(S)}}, \quad (\text{D11})$$

$$b_1 = \frac{\delta_2^{(S)}\delta_5^{(S)} - \delta_3^{(S)}\delta_4^{(S)}}{\{\delta_3^{(S)}\}^2 - \delta_2^{(S)}\delta_4^{(S)}}, \quad (\text{D12})$$

$$b_2 = \frac{\{\delta_4^{(S)}\}^2 - \delta_3^{(S)}\delta_5^{(S)}}{\{\delta_3^{(S)}\}^2 - \delta_2^{(S)}\delta_4^{(S)}}. \quad (\text{D13})$$

## APPENDIX E: IMPACT OF EFT CORRECTIONS ON GridSPT POWER SPECTRA AT ONE-LOOP ORDER

Throughout the paper, our main focus is on the field-level implementation of the RSD on the SPT calculations, leaving other implementations such as the galaxy bias and the effective-field-theory treatment to future works. Nevertheless, it is interesting to see how their systematics can change the GridSPT results in the main text. In this appendix, we examine the effective-field-theory (EFT) treatment and discuss the impact of EFT counterterms on the GridSPT power spectra at one-loop order.

The EFT treatment provides a systematic way to mitigate the UV-sensitive behaviors inherent in the SPT by introducing counterterms. At one-loop order in redshift space, the multipole moments of the SPT matter power spectrum given in Eq. (25) are modified to (e.g., Refs. [96–98])

$$\begin{aligned} P_{\ell,\text{SPT}}^{(S)}(k) &= P_{\ell,\text{lin}}^{(S)}(k) + P_{\ell,1\text{-loop}}^{(S)}(k) \\ \rightarrow P_{\ell,\text{EFT}}^{(S)}(k) &= P_{\ell,\text{lin}}^{(S)}(k) + P_{\ell,1\text{-loop}}^{(S)}(k) - 2c_{\ell,\text{eff}}^2 k^2 P_{\text{lin}}(k), \end{aligned} \quad (\text{E1})$$

where the last term in the second line is the EFT counterterm, which suppresses the power spectrum amplitude. With the scale-dependent suppression, the counterterm can mitigate the UV-sensitive behaviors. In Eq. (E1), the parameters originally introduced in Ref. [96] are redefined, and are summarized for each multipole as  $c_{\ell,\text{eff}}$ . Given the measured power spectra from  $N$ -body simulations, these parameters are separately and uniquely determined by comparing those with Eq. (E1) constructed from the GridSPT results.

In Fig. 19, using the one-loop GridSPT results shown in Figs. 5 and 7, the power spectra  $P_{\ell,\text{EFT}}^{(S)}$  are obtained, and they are plotted as green dashed lines, together with the  $N$ -body (solid filled square) and GridSPT results without the EFT corrections (green solid). Here, the calibrated results of the EFT parameters, indicated in each panel, are obtained by fitting the  $N$ -body results to GridSPT data below the cutoff scale  $k_{\text{max}} = 0.25h \text{ Mpc}^{-1}$ .<sup>14</sup> The EFT power spectra agree well with simulation results at  $k \lesssim k_{\text{max}}$ . The resultant EFT parameters are close to each other between the two panels, where the GridSPT results with different resolutions (upper:  $N_{\text{grid}} = 1200^3$ ; lower:  $N_{\text{grid}} = 600^3$ ) are used to construct the EFT spectra. These are indeed consistent with those found in the literature (e.g., Refs. [98,99]). In Fig. 20, we also examine the cutoff dependence of the EFT parameters, the results of which are plotted as a function of  $k_{\text{max}}$ . This shows that the EFT parameters calibrated from  $N$ -body and GridSPT results are rather insensitive to the cutoff scales, again consistent with those found in previous works.

Finally, a closer look at EFT predictions in Fig. 19 reveals that a prominent wiggle feature, arising from the baryon acoustic oscillations, still remains visible even beyond  $k_{\text{max}}$ . This implies that adding only the counterterms does not fully describe the nonlinear smearing effect of baryon acoustic oscillations, which are clearly seen in the  $N$ -body simulations. The results suggest that the IR resummation at the field level is crucial to further improve

<sup>14</sup>In our case with a single free parameter, given the  $N$ -body and GridSPT power spectra,  $P_{\ell,\text{N-body}}^{(S)}$ ,  $P_{\ell,\text{SPT}}^{(S)}$ , and  $P_{\text{lin}}$ , the EFT parameters are determined uniquely from

$$c_{\ell,\text{eff}}^2 = \frac{1}{2} \frac{\sum_{k_i \leq k_{\text{max}}} \frac{k_i^2 P_{\text{lin}}(k_i)}{[\Delta P_{\ell,\text{N-body}}^{(S)}(k_i)]^2} [P_{\ell,\text{SPT}}^{(S)}(k_i) - P_{\ell,\text{N-body}}^{(S)}(k_i)]}{\sum_{k_j \leq k_{\text{max}}} \frac{\{k_j^2 P_{\text{lin}}(k_j)\}^2}{[\Delta P_{\ell,\text{N-body}}^{(S)}(k_j)]^2}}, \quad (\text{E2})$$

where the quantity  $\Delta P_{\ell,\text{N-body}}^{(S)}(k)$  is the error of the  $N$ -body simulations, for which we adopt the sampling error estimated from the number of Fourier modes.

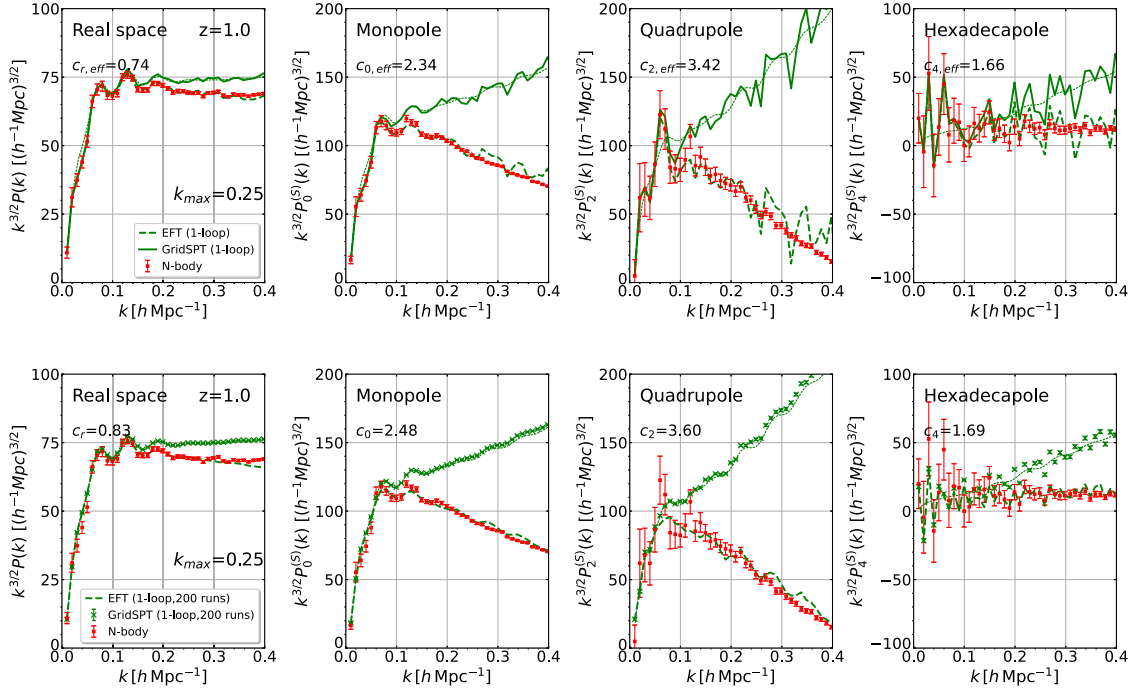


FIG. 19. Real- and redshift-space power spectra at  $z = 1$  obtained from the GridSPT calculations at one-loop order, taking the EFT corrections into account. The dashed lines are the GridSPT one-loop spectra including the EFT counterterms [see Eq. (E1)]. Adopting the EFT parameters calibrated with  $N$ -body simulations at  $k \leq k_{\max} = 0.25 h \text{ Mpc}^{-1}$ , the results shown in the upper and lower panels are obtained in the same setup as shown in Figs. 5 and 7, respectively. The EFT parameters used in the plot,  $c_{\ell, \text{eff}}$ , are indicated in each panel in units of  $h \text{ Mpc}^{-1}$ . For comparison, we also plot the results of  $N$ -body simulations (filled squares), GridSPT (solid lines or crosses), and analytical SPT (thin dotted lines) one-loop calculations without EFT corrections, which are taken from Figs. 5 and 7. Note that all of the power spectra are multiplied by  $k^{3/2}$ .

the predictions. In Refs. [72,74], the field-level IR resummation was considered in the framework of the Lagrangian PT, and it was implemented based on the hybrid scheme

that combines both the grid- and particle-based methods. Since the displacement fields in Lagrangian PT calculations are linked to the SPT density fields, in combination with the

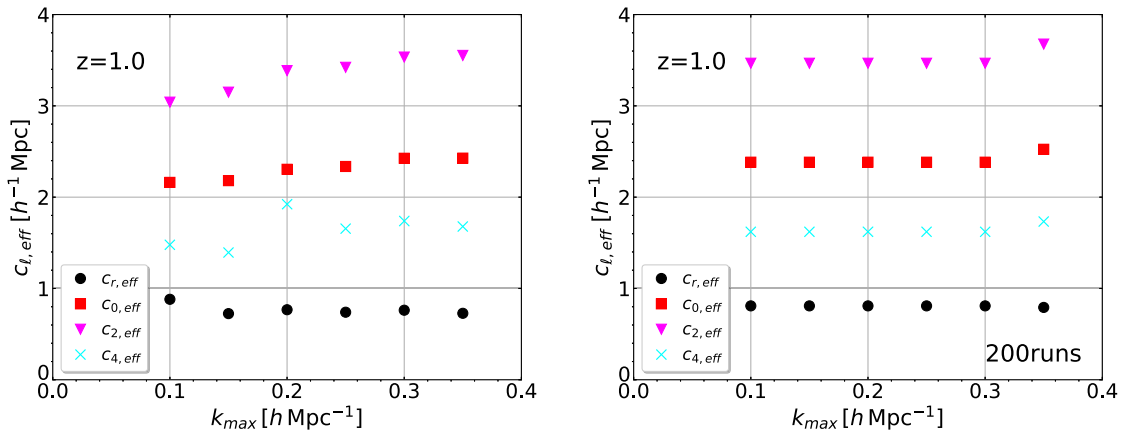


FIG. 20. Dependence of the EFT parameters  $c_{\ell, \text{eff}}$  on the cutoff scale  $k_{\max}$  at  $z = 1$ . Using the GridSPT and  $N$ -body data set shown in Figs. 5 and 7, each of the EFT parameters given in real and redshift space [Eq. (E1)] is independently calibrated according to Eq. (E2), and the results are presented in the left and right panels, respectively, as a function of the cutoff wave number  $k_{\max}$ . While the filled circles represent the real-space EFT parameter  $c_{r, \text{eff}}$ , filled squares, filled triangles, and crosses are the redshift-space EFT parameters for the monopole, quadrupole, and hexadecapole moments ( $c_{0, \text{eff}}$ ,  $c_{2, \text{eff}}$ , and  $c_{4, \text{eff}}$ ), respectively.

particle-based method, the IR-resummed density field can also be generated with the GridSPT calculations. On the other hand, a proper way to treat the field-level IR resummation with only the grid-based method needs further investigation, and we leave it to future studies.

### APPENDIX F: ON THE IR SENSITIVITY OF GridSPT CALCULATIONS

As we discussed in the main text and Appendix C, in addition to the UV sensitivity, the SPT calculations intrinsically possess an IR-sensitive behavior. In particular, for the scale-free linear power spectrum of  $P_{\text{lin}} \propto k^n$  with  $n < -1$ , each of the loop integrals is known to exhibit an IR divergence. However, summing up the contributions order by order, these divergences are exactly canceled out [25,100–102]. This is known as a consequence of the Galilean invariance. Although the IR divergence does not occur in reality for the  $\Lambda$ CDM-like linear power spectrum, a large cancellation of the loop integrals still remains significant, and hence the IR-safe integration technique needs to be implemented for an accurate analytical SPT calculation (e.g., Refs. [67,103]).

Here we discuss the IR sensitivity of the GridSPT calculations, and try to see its impact by computing separately the higher-order corrections to the SPT power spectrum. For this purpose, we consider three different box sizes of  $L_{\text{box}} = 600, 1000, \text{ and } 1300 h^{-1}$  Mpc, and the GridSPT calculations are performed for each cubic box

over 200 realizations, adopting  $N_{\text{grid}} = 360^3, 600^3, \text{ and } 780^3$ , respectively. With this setup, the Nyquist frequency becomes  $k_{\text{Nyq}} \simeq 1.88 h \text{ Mpc}^{-1}$  for all three cases, and using the 1/3 rule for the aliasing correction, the GridSPT results have the same resolution up to  $k_{\text{crit}} \simeq 0.62 h \text{ Mpc}^{-1}$ , as we examined in Figs. 7 and 8.

Figure 21 shows the results of the one- (upper) and two-loop (lower) corrections to the power spectra at  $z = 1$ . Each of the SPT corrections [ $P_{ab}^{(S)}$  as defined in Eq. (32)] is separately measured, and by applying the multipole expansion in redshift space, the absolute values of the power spectra averaged over 200 realizations are plotted on logarithmic scales, together with the standard error of the mean. On top of the strong scale-dependent behavior of each contribution having a positive or negative amplitude, a careful look at the two-loop corrections reveals a small but visible systematic trend in both real and redshift space. That is, the absolute values of the two-loop corrections are systematically reduced when decreasing the box size, resulting in  $\sim 5\%$  change in amplitude between the results with  $L_{\text{box}} = 600$  and  $1300 h^{-1}$  Mpc. This is indeed expected from the IR-sensitive behaviors, and is consistent with analytical SPT predictions.

In Fig. 22, summing up each contribution in Fig. 21, the total one- and two-loop corrections [as defined in Eqs. (27) and (28)] are shown. Due to a large cancellation, the resultant amplitude of the loop corrections,  $P_{1\text{-loop}}^{(S)}$  and  $P_{2\text{-loop}}^{(S)}$ , is significantly reduced, and here we plot them on

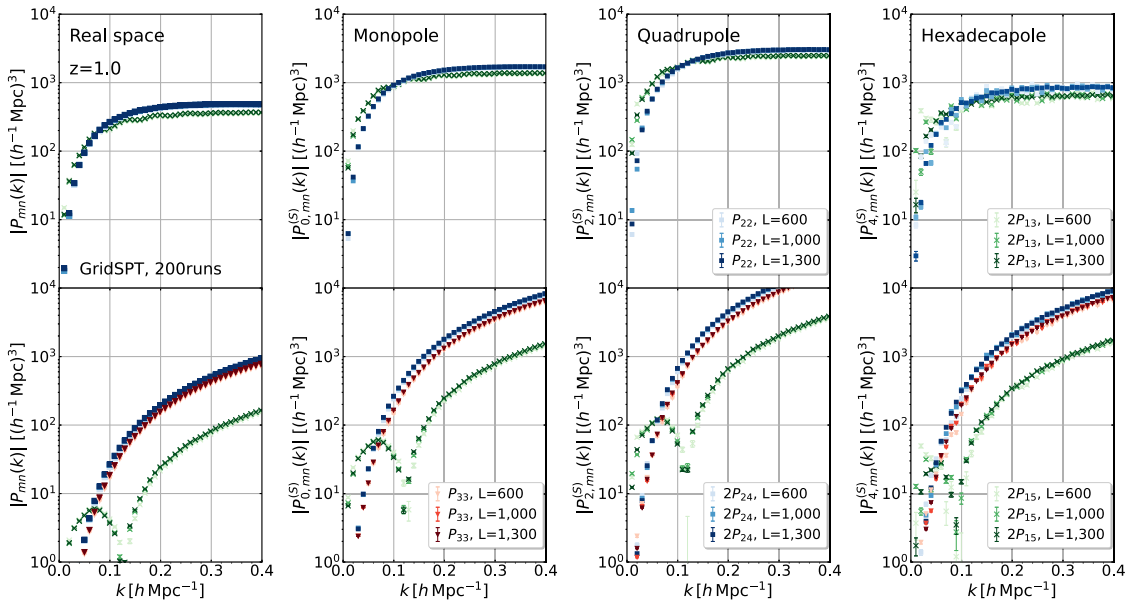


FIG. 21. Sensitivity of the SPT power spectrum corrections to the low- $k$  cutoff at  $z = 1$ . Varying the box size  $L_{\text{box}}$  from 600 to  $1300 h^{-1}$  Mpc, the GridSPT results of the one-loop (upper) and two-loop (lower) corrections to the real- and redshift-space power spectra, averaged over 200 realizations, are plotted separately. From left to right, the absolute values of the real-space power spectra, monopole, quadrupole, and hexadecapole moments of redshift-space power spectra are shown. The error bars indicate the standard error of the mean. Note that the resolution of GridSPT calculations is kept fixed for three different box sizes by changing the number of grids:  $N_{\text{grid}} = 360, 600, \text{ and } 780$  for  $L_{\text{box}} = 600, 1000, \text{ and } 1300 h^{-1}$  Mpc.

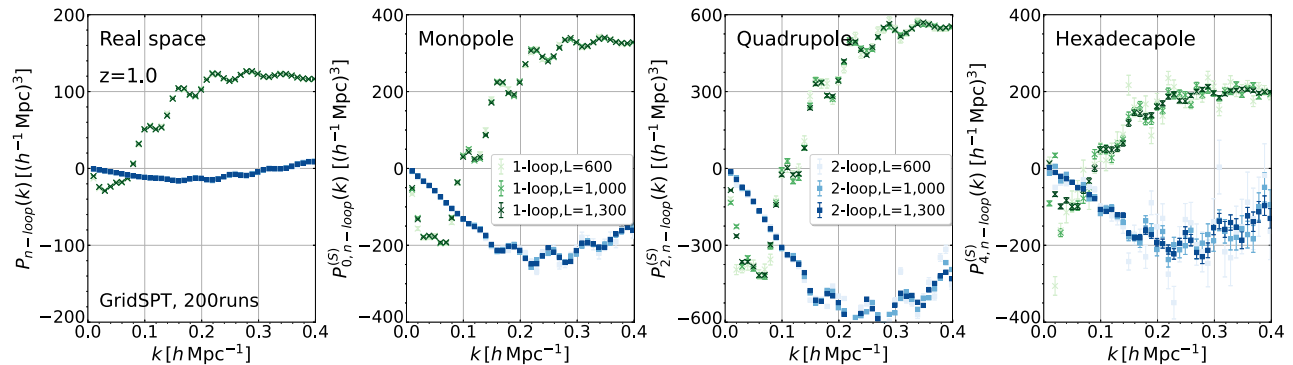


FIG. 22. Dependence of the one-loop (green) and two-loop (blue) power spectrum corrections on the box size of GridSPT calculations at  $z = 1$ . Summing up each contribution in Fig. 21, the spectra,  $P_{1\text{-loop}}^{(S)}$  and  $P_{2\text{-loop}}^{(S)}$  [defined in Eqs. (27) and (28)] are computed. Then, from left to right, the real-space power spectra, monopole, quadrupole, and hexadecapole moments of redshift-space power spectra, averaged over 200 realizations, are plotted, together with the error bars indicating the standard errors of the mean. Different colors represent the GridSPT results with different box sizes:  $L_{\text{box}} = 600, 1000,$  and  $1300h^{-1}$  Mpc from lighter to darker colors.

a linear scale. Apart from some variations over the results with different  $L_{\text{box}}$ , which look prominent for higher multipoles, there is no clear systematic dependence on the box size, compared to the trend seen in each building block. We have also checked the results in individual

realizations and again found no systematic dependence on the box size. This implies that the Galilean invariance is properly ensured in the GridSPT calculations, and the IR sensitivity disappears after summing up loop corrections.

- [1] V. Desjacques, D. Jeong, and F. Schmidt, *Phys. Rep.* **733**, 1 (2018).
- [2] K. Gebhardt *et al.*, *Astrophys. J.* **923**, 217 (2021).
- [3] M. Takada *et al.*, *Publ. Astron. Soc. Jpn.* **66**, R1 (2014).
- [4] DESI Collaboration, [arXiv:1611.00036](https://arxiv.org/abs/1611.00036).
- [5] R. Laureijs *et al.*, [arXiv:1110.3193](https://arxiv.org/abs/1110.3193).
- [6] J. Green *et al.*, [arXiv:1208.4012](https://arxiv.org/abs/1208.4012).
- [7] O. Doré *et al.*, [arXiv:1805.05489](https://arxiv.org/abs/1805.05489).
- [8] D. H. Weinberg, M. J. Mortonson, D. J. Eisenstein, C. Hirata, A. G. Riess, and E. Rozo, *Phys. Rep.* **530**, 87 (2013).
- [9] M. Crocce and R. Scoccimarro, *Phys. Rev. D* **73**, 063519 (2006).
- [10] D. Jeong and E. Komatsu, *Astrophys. J.* **651**, 619 (2006).
- [11] D. Jeong and E. Komatsu, *Astrophys. J.* **691**, 569 (2009).
- [12] M. Crocce and R. Scoccimarro, *Phys. Rev. D* **77**, 023533 (2008).
- [13] A. Taruya and T. Hiramatsu, *Astrophys. J.* **674**, 617 (2008).
- [14] T. Matsubara, *Phys. Rev. D* **77**, 063530 (2008).
- [15] F. Bernardeau, M. Crocce, and R. Scoccimarro, *Phys. Rev. D* **78**, 103521 (2008).
- [16] T. Nishimichi *et al.*, *Publ. Astron. Soc. Jpn.* **61**, 321 (2009).
- [17] E. Lawrence, K. Heitmann, M. White, D. Higdon, C. Wagner, S. Habib, and B. Williams, *Astrophys. J.* **713**, 1322 (2010).
- [18] A. Taruya, T. Nishimichi, and S. Saito, *Phys. Rev. D* **82**, 063522 (2010).
- [19] T. Nishimichi and A. Taruya, *Phys. Rev. D* **84**, 043526 (2011).
- [20] D. Baumann, A. Nicolis, L. Senatore, and M. Zaldarriaga, *J. Cosmol. Astropart. Phys.* **07** (2012) 051.
- [21] L. Senatore, *J. Cosmol. Astropart. Phys.* **11** (2015) 007.
- [22] M. Mirbabayi, F. Schmidt, and M. Zaldarriaga, *J. Cosmol. Astropart. Phys.* **07** (2015) 030.
- [23] T. Nishimichi, F. Bernardeau, and A. Taruya, *Phys. Rev. D* **96**, 123515 (2017).
- [24] T. Nishimichi, M. Takada, R. Takahashi, K. Osato, M. Shirasaki, T. Oogi, H. Miyatake, M. Oguri, R. Murata, Y. Kobayashi, and N. Yoshida, *Astrophys. J.* **884**, 29 (2019).
- [25] F. Bernardeau, S. Colombi, E. Gaztanaga, and R. Scoccimarro, *Phys. Rep.* **367**, 1 (2002).
- [26] A. Taruya, T. Nishimichi, and D. Jeong, *Phys. Rev. D* **98**, 103532 (2018).
- [27] N. Roth and C. Porciani, *Mon. Not. R. Astron. Soc.* **415**, 829 (2011).
- [28] S. Tassev, *J. Cosmol. Astropart. Phys.* **06** (2014) 008.
- [29] A. Taruya, T. Nishimichi, and D. Jeong, *Phys. Rev. D* **103**, 023501 (2021).
- [30] P. J. E. Peebles, *The Large-Scale Structure of the Universe* (Princeton University Press, Princeton, NJ, 1980).
- [31] A. J. S. Hamilton, Linear redshift distortions: A review, in *The Evolving Universe*, Astrophysics and Space Science Library, Vol. 231, edited by D. Hamilton (Kluwer Academic Publishers, Dordrecht, 1998), p. 185, [https://doi.org/10.1007/978-1-4020-0804-0\\_10](https://doi.org/10.1007/978-1-4020-0804-0_10).

- link.springer.com/chapter/10.1007%2F978-94-011-4960-0\_17.
- [32] R. Scoccimarro, *Phys. Rev. D* **70**, 083007 (2004).
- [33] Z. Vlah, U. Seljak, P. McDonald, T. Okumura, and T. Baldauf, *J. Cosmol. Astropart. Phys.* **11** (2012) 009.
- [34] A. Taruya, T. Nishimichi, and F. Bernardeau, *Phys. Rev. D* **87**, 083509 (2013).
- [35] Z. Vlah, U. Seljak, T. Okumura, and V. Desjacques, *J. Cosmol. Astropart. Phys.* **10** (2013) 053.
- [36] J. Carlson, B. Reid, and M. White, *Mon. Not. R. Astron. Soc.* **429**, 1674 (2013).
- [37] L. Wang, B. Reid, and M. White, *Mon. Not. R. Astron. Soc.* **437**, 588 (2014).
- [38] T. Matsubara, *Phys. Rev. D* **90**, 043537 (2014).
- [39] N. Hand, U. Seljak, F. Beutler, and Z. Vlah, *J. Cosmol. Astropart. Phys.* **10** (2017) 009.
- [40] Z. Vlah and M. White, *J. Cosmol. Astropart. Phys.* **03** (2019) 007.
- [41] S.-F. Chen, Z. Vlah, E. Castorina, and M. White, *J. Cosmol. Astropart. Phys.* **03** (2021) 100.
- [42] J. J. M. Carrasco, M. P. Hertzberg, and L. Senatore, *J. High Energy Phys.* **09** (2012) 82.
- [43] T. Baldauf, L. Mercolli, and M. Zaldarriaga, *Phys. Rev. D* **92**, 123007 (2015).
- [44] T. Nishimichi, G. D'Amico, M. M. Ivanov, L. Senatore, M. Simonović, M. Takada, M. Zaldarriaga, and P. Zhang, *Phys. Rev. D* **102**, 123541 (2020).
- [45] T. Steele and T. Baldauf, *Phys. Rev. D* **103**, 023520 (2021).
- [46] T. Steele and T. Baldauf, *Phys. Rev. D* **103**, 103518 (2021).
- [47] M. Pietroni, *J. Cosmol. Astropart. Phys.* **10** (2008) 036.
- [48] R. Takahashi, *Prog. Theor. Phys.* **120**, 549 (2008).
- [49] T. Hiramatsu and A. Taruya, *Phys. Rev. D* **79**, 103526 (2009).
- [50] D. Blas, M. Garny, and T. Konstandin, *J. Cosmol. Astropart. Phys.* **01** (2014) 010.
- [51] F. Bernardeau, A. Taruya, and T. Nishimichi, *Phys. Rev. D* **89**, 023502 (2014).
- [52] T. Nishimichi, F. Bernardeau, and A. Taruya, *Phys. Lett. B* **762**, 247 (2016).
- [53] N. Kaiser, *Mon. Not. R. Astron. Soc.* **227**, 1 (1987).
- [54] S. Cole, K. B. Fisher, and D. H. Weinberg, *Mon. Not. R. Astron. Soc.* **267**, 785 (1994).
- [55] A. Raccanelli, D. Bertacca, D. Jeong, M. C. Neyrinck, and A. S. Szalay, *Phys. Dark Universe* **19**, 109 (2018).
- [56] V. Springel, *Mon. Not. R. Astron. Soc.* **364**, 1105 (2005).
- [57] M. Crocce, S. Pueblas, and R. Scoccimarro, *Mon. Not. R. Astron. Soc.* **373**, 369 (2006).
- [58] D. Jeong, L. Dai, M. Kamionkowski, and A. S. Szalay, *Mon. Not. R. Astron. Soc.* **449**, 3312 (2015).
- [59] S. Tanaka, K. Yoshikawa, T. Minoshima, and N. Yoshida, *Astrophys. J.* **849**, 76 (2017).
- [60] E. Sefusatti, M. Crocce, R. Scoccimarro, and H. Couchman, *Mon. Not. R. Astron. Soc.* **460**, 3624 (2016).
- [61] I. Hashimoto, Y. Rasera, and A. Taruya, *Phys. Rev. D* **96**, 043526 (2017).
- [62] R. Scoccimarro, H. M. P. Couchman, and J. A. Frieman, *Astrophys. J.* **517**, 531 (1999).
- [63] R. Scoccimarro, *Phys. Rev. D* **92**, 083532 (2015).
- [64] P. Gagrani and L. Samushia, *Mon. Not. R. Astron. Soc.* **467**, 928 (2017).
- [65] K. Yamamoto, Y. Nan, and C. Hikage, *Phys. Rev. D* **95**, 043528 (2017).
- [66] N. S. Sugiyama, S. Saito, F. Beutler, and H.-J. Seo, *Mon. Not. R. Astron. Soc.* **484**, 364 (2019).
- [67] T. Baldauf, L. Mercolli, M. Mirbabayi, and E. Pajer, *J. Cosmol. Astropart. Phys.* **05** (2015) 007.
- [68] D. Bianchi, H. Gil-Marín, R. Ruggeri, and W. J. Percival, *Mon. Not. R. Astron. Soc.: Lett.* **453**, L11 (2015).
- [69] P. J. E. Peebles and J. T. Yu, *Astrophys. J.* **162**, 815 (1970).
- [70] D. J. Eisenstein and W. Hu, *Astrophys. J.* **496**, 605 (1998).
- [71] A. Taruya, F. Bernardeau, T. Nishimichi, and S. Codis, *Phys. Rev. D* **86**, 103528 (2012).
- [72] M. Schmittfull, M. Simonović, V. Assassi, and M. Zaldarriaga, *Phys. Rev. D* **100**, 043514 (2019).
- [73] C. Modi, M. White, A. Slosar, and E. Castorina, *J. Cosmol. Astropart. Phys.* **11** (2019) 023.
- [74] M. Schmittfull, M. Simonović, M. M. Ivanov, O. H. E. Philcox, and M. Zaldarriaga, *J. Cosmol. Astropart. Phys.* **05** (2021) 059.
- [75] M. Davis and P. J. E. Peebles, *Astrophys. J.* **267**, 465 (1983).
- [76] J. C. Jackson, *Mon. Not. R. Astron. Soc.* **156**, 1P (1972).
- [77] T. Okumura, U. Seljak, P. McDonald, and V. Desjacques, *J. Cosmol. Astropart. Phys.* **02** (2012) 010.
- [78] A. Yoshisato, T. Matsubara, and M. Morikawa, *Astrophys. J.* **498**, 48 (1998).
- [79] T. Matsubara, A. Yoshisato, and M. Morikawa, *Astrophys. J.* **504**, 7 (1998).
- [80] T. Tatekawa, *Phys. Rev. D* **75**, 044028 (2007).
- [81] E. J. Hinch, *Perturbation Methods* (Cambridge University Press, Cambridge, England, 1991).
- [82] P. McDonald and A. Roy, *J. Cosmol. Astropart. Phys.* **08** (2009) 020.
- [83] K. C. Chan, R. Scoccimarro, and R. K. Sheth, *Phys. Rev. D* **85**, 083509 (2012).
- [84] S. Saito, T. Baldauf, Z. Vlah, U. Seljak, T. Okumura, and P. McDonald, *Phys. Rev. D* **90**, 123522 (2014).
- [85] T. Fujita and Z. Vlah, *J. Cosmol. Astropart. Phys.* **10** (2020) 059.
- [86] F. S. Kitaura and T. A. Enßlin, *Mon. Not. R. Astron. Soc.* **389**, 497 (2008).
- [87] J. Jasche and B. D. Wandelt, *Mon. Not. R. Astron. Soc.* **432**, 894 (2013).
- [88] F. Schmidt, F. Elsner, J. Jasche, N. M. Nguyen, and G. Lavaux, *J. Cosmol. Astropart. Phys.* **01** (2019) 042.
- [89] S. A. Orszag, *J. Atmos. Sci.* **28**, 1074 (1971).
- [90] R. Takahashi *et al.*, *Mon. Not. R. Astron. Soc.* **389**, 1675 (2008).
- [91] M. H. Goroff, B. Grinstein, S. J. Rey, and M. B. Wise, *Astrophys. J.* **311**, 6 (1986).
- [92] B. Jain and E. Bertschinger, *Astrophys. J.* **431**, 495 (1994).
- [93] R. Scoccimarro, M. Zaldarriaga, and L. Hui, *Astrophys. J.* **527**, 1 (1999).
- [94] T. Hahn, *Comput. Phys. Commun.* **168**, 78 (2005).
- [95] T. Konstandin, R. A. Porto, and H. Rubira, *J. Cosmol. Astropart. Phys.* **11** (2019) 027.
- [96] L. Senatore and M. Zaldarriaga, arXiv:1409.1225.
- [97] M. Lewandowski, L. Senatore, F. Prada, C. Zhao, and C.-H. Chuang, *Phys. Rev. D* **97**, 063526 (2018).

- 
- [98] L. Fonseca de la Bella, D. Regan, D. Seery, and S. Hotchkiss, *J. Cosmol. Astropart. Phys.* **11** (2017) 039.
- [99] T. Lazeyras and F. Schmidt, *J. Cosmol. Astropart. Phys.* **11** (2019) 041.
- [100] N. Makino, M. Sasaki, and Y. Suto, *Phys. Rev. D* **46**, 585 (1992).
- [101] R. Scoccimarro and J. Frieman, *Astrophys. J.* **473**, 620 (1996).
- [102] B. Jain and E. Bertschinger, *Astrophys. J.* **456**, 43 (1996).
- [103] J. J. M. Carrasco, S. Foreman, D. Green, and L. Senatore, *J. Cosmol. Astropart. Phys.* **07** (2014) 056.